Geophysical Journal International

Geophys. J. Int. (2013) **193,** 920–937 doi: 10.1093/gji/ggt010

A new catalogue of normal-mode splitting function measurements up to 10 mHz

Arwen Deuss,[1] Jeroen Ritsema[2] and Hendrik van Heijst[3]

[1] *Bullard Labs, University of Cambridge, Madingley Road, Cambridge, UK. E-mail: afd28@cam.ac.uk*
[2] *Department of Earth and Environmental Sciences, University of Michigan, Ann Arbor, MI, USA*
[3] *Department of Earth Sciences, University of Oxford, Oxford, UK*

Accepted 2013 January 11. Received 2013 January 11; in original form 2012 July 11

SUMMARY

The splitting of the Earth's free-oscillation spectra places important constraints on the wave speed and density structure of the Earth's mantle and core. We present a new set of 164 self-coupled and 32 cross-coupled splitting functions. They are derived from modal spectra up to 10 mHz for 91 events with $M_w \geq 7.4$ from the last 34 yr (1976–2010). Our data include the 2001 June 23 Peru event ($M_w = 8.4$), the Sumatra events of 2004 ($M_w = 9.0$) and 2005 ($M_w = 8.6$), the 2008 Wenchuan, China event ($M_w = 7.9$) and the 2010 Chile event ($M_w = 8.8$). The new events provide significant improvement of data coverage particularly in continental areas. Almost half of the splitting functions have never been measured before. In particular, we measured 33 new modes sensitive to mantle compressional wave velocity, 10 new inner-core sensitive modes and 22 new cross-coupled splitting functions. These provide new constraints on the large-scale compressional structure of the mantle and the odd-degree structure of the mantle and inner core and can be used in future inversions of heterogeneous Earth structure. Our new splitting function coefficient data set will be available online.

Key words: Surface waves and free oscillations; Seismic anisotropy; Seismic tomography; Mantle processes; Core, outer core and inner core.

1 INTRODUCTION

Measurements of the splitting of long-period free-oscillation spectra provide important constraints on the Earth's 3-D wave speed structure on scale lengths comparable to the Earth's radius. In addition, normal-mode data are the only available seismic data to constrain aspherical density structure (Ishii & Tromp 1999; Resovsky & Trampert 2003; Trampert *et al.* 2004), albeit that trade-offs arise with mantle velocity structure (Resovsky & Ritzwoller 1999b; Romanowicz 2001; Kuo & Romanowicz 2002). Nevertheless, normal-mode analyses have indicated an anticorrelation between shear wave velocity and density perturbation in the lowermost mantle beneath Africa and the Pacific. This has had a profound influence on our understanding of the thermo-chemical structure and dynamics of the mantle, as it suggests the existence of compositional heterogeneity in the lower most mantle. New normal-mode measurements are essential to improve constraints on mantle velocity and density structure and further our understanding of mantle dynamics and it is hoped that our new data set will improve the reliability and robustness of tomographic models of aspherical density structure.

It is common to measure splitting function coefficients from normal-mode spectra using least-squares inversion (Woodhouse & Giardini 1985; Woodhouse *et al.* 1986; Ritzwoller *et al.* 1986, 1988; Giardini *et al.* 1987, 1988; He & Tromp 1996; Resovsky & Ritzwoller 1998; Durek & Romanowicz 1999; Masters *et al.* 2000b). Splitting function coefficients are linearly dependent upon the Earth's aspherical velocity and density structure. They have been used in tomographic inversions to obtain 3-D velocity and density models (e.g. Li *et al.* 1991; Resovsky & Ritzwoller 1999a; Ishii & Tromp 1999; Trampert *et al.* 2004), often in combination with travelling wave data (e.g. Ritsema *et al.* 1999, 2011; Masters *et al.* 2000a).

The most recent compilations of splitting functions are now more than 10 yr old (He & Tromp 1996; Resovsky & Ritzwoller 1998; Durek & Romanowicz 1999; Masters *et al.* 2000b). However, several large earthquakes have occurred (see Fig. 1 and Table 1) and the global network of seismic stations has expanded since then. Thus, it is timely to update the measurement of normal-mode splitting functions. We have already published new measurements of the longest period normal modes that had never been measured before using seismometers, including ${}_0S_2$ and ${}_2S_1$ (Deuss *et al.* 2011). Here we present a new compilation of splitting functions that is almost twice as large as earlier studies, especially in the 4–10 mHz frequency range (see Fig. 2a). A large number of the new modes are sensitive to compressional velocity (v_p) structure in the mantle (Fig. 2b). Some of these v_p sensitive modes were measured by Resovsky & Pestana (2003); here we will greatly expand the number of observed splitting functions for v_p sensitive modes of the mantle. We will also add previously unmeasured mantle shear wave velocity (v_s) sensitive modes and inner-core sensitive modes (Fig. 2c).

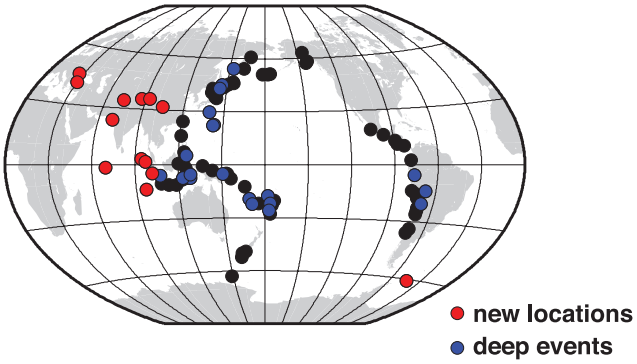

Figure 1. Locations of the 91 events used in this study. The red circles denote events in continental locations where previous splitting function studies did not have any events; the blue circles indicate events which are deeper than 100 km.

Table 1. List of events used in this study. Date is day/month/year, depth is in km, M_w is the moment magnitude from the CMT catalogue and N_s denotes the number of stations used per event.

Date	Location	Depth	M_w	N_s
16/08/1976	Mindanao Philippines	33.0	8.0	3
30/11/1976	Chile Bolivia	133.7	7.5	3
04/03/1977	Romania	83.6	7.5	5
22/06/1977	Tonga Islands	61.3	8.0	7
19/08/1977	Sumbawa Island	23.3	8.3	7
12/06/1978	Honshu Japan	37.7	7.6	3
29/11/1978	Oaxaca Mexico	16.1	7.7	8
06/12/1978	Kurils Islands	181.0	7.8	11
12/12/1979	Ecuador	19.7	8.1	9
17/07/1980	Santa Cruz Islands	34.0	7.7	9
25/05/1981	New Zealand	33.3	7.6	12
22/06/1982	Banda Sea	473.4	7.4	9
18/03/1983	New Ireland	69.6	7.7	15
26/05/1983	Honshu Japan	12.6	7.7	12
04/10/1983	Coast of Chile	38.7	7.6	9
24/11/1983	Banda Sea	157.1	7.4	10
06/03/1984	Honshu Japan	446.0	7.4	7
20/11/1984	Mindanao	180.7	7.5	12
03/03/1985	Central Chile	40.7	7.9	8
07/05/1986	Andreanof Islands	31.3	7.9	11
20/10/1986	Kermadec Islands	50.4	7.7	11
30/11/1987	Gulf of Alaska	15.0	7.8	19
06/03/1988	Gulf of Alaska	15.0	7.7	19
23/05/1989	Macquarie Islands	15.0	8.0	24
03/03/1990	South of Fiji	25.3	7.6	23
18/04/1990	Minahassa	33.2	7.6	24
16/07/1990	Luzon Philippines	15.0	7.7	21
30/12/1990	New Britain	204.8	7.4	14
22/04/1991	Costa Rica	15.0	7.6	24
22/12/1991	Kuril Islands	31.2	7.6	17
02/09/1992	Nicaragua	15.0	7.6	30
11/10/1992	Vanuatu	141.1	7.4	32
12/12/1992	Flores Island	20.4	7.7	36
15/01/1993	Hokkaido Japan	100.0	7.6	27
12/07/1993	Hokkaido Japan	16.5	7.7	46
03/03/1994	Fiji Islands	567.8	7.6	54
02/06/1994	South of Java	15.0	7.8	31
09/06/1994	Northern Bolivia	647.1	8.3	56
04/10/1994	Kuril Islands	68.2	8.3	46
28/12/1994	Coast of Honshu	27.7	7.7	50
30/07/1995	Northern Chili	28.7	8.0	50
09/10/1995	Jalisco Mexico	15.0	8.0	46
03/12/1995	Kurile Islands	25.9	7.9	44
01/01/1996	Minahassa Peninsula	15.0	7.9	24
17/02/1996	West Irian	15.0	8.2	63
10/06/1996	Andrean of Islands	29.0	7.9	33
17/06/1996	Flores Sea	584.2	7.8	53
12/11/1996	Coast of Peru	37.4	7.7	59
14/10/1997	South of Fiji Islands	165.9	7.7	42
08/11/1997	Tibet	16.4	7.5	61
05/12/1997	Kamchatka	33.6	7.8	41
04/01/1998	Loyalty Islands	114.3	7.4	35
25/03/1998	Balleny Islands	28.8	8.1	66
29/11/1998	Ceram Sea	16.4	7.7	53
17/08/1999	Turkey	17.0	7.6	63
20/09/1999	Taiwan	21.2	7.6	67
28/03/2000	Volcano Island	99.7	7.6	63
04/06/2000	Southern Sumatra	43.9	7.8	91
18/06/2000	South Indian Ocean	15.0	7.9	88
13/01/2001	El Salvador	56.0	7.7	61
26/01/2001	India	19.8	7.6	66
23/06/2001	Coast of Peru	29.6	8.4	88
07/07/2001	Coast of Peru	25.0	7.6	44
14/11/2001	Qinghai China	15.0	7.8	65
08/09/2002	Papua New Guinea	19.5	7.6	50
03/11/2002	Central Alaska	15.0	7.8	72
15/07/2003	Carlsberg Ridge	15.0	7.5	64
04/08/2003	Scotia Sea	15.0	7.6	61
25/09/2003	Hokkaido Japan	28.2	8.3	88
17/11/2003	Rat Islands	21.7	7.7	60
23/12/2004	North Macquarie	27.5	8.1	87
26/12/2004	Northern Sumatra	28.6	9.0	85
28/03/2005	Northern Sumatra	25.8	8.6	91
09/09/2005	New Ireland	83.6	7.6	59
26/09/2005	Northern Peru	108.1	7.5	63
08/10/2005	Pakistan	12.0	7.6	80
27/01/2006	Banda Sea	379.4	7.6	75
20/04/2006	Eastern Siberia	12.0	7.6	65
03/05/2006	Tonga Islands	67.8	8.0	43
17/07/2006	South of Java	20.0	7.7	60
15/11/2006	Kuril Islands	13.5	8.3	69
13/01/2007	East Kuril	12.0	8.1	58
01/04/2007	Solomon Islands	14.1	8.1	48
08/08/2007	Java Indonesia	304.8	7.5	49
15/08/2007	Coast of Peru	33.8	8.0	50
28/09/2007	Volcano Japan	275.8	7.5	54
14/11/2007	Northern Chile	37.6	7.7	50
09/12/2007	South of Fiji Islands	149.9	7.8	45
12/05/2008	Sichuan China	12.0	7.9	71
05/07/2008	Sea of Okhotsk	615.2	7.7	64
27/02/2010	Chile	23.2	8.8	129

2 THEORY AND METHOD

2.1 Normal-mode splitting functions

Normal modes are standing waves along the surface and radius of the Earth. The observations and modelling of normal modes require day-long, high signal-to-noise waveform data generated by large ($M_w > 7.5$) earthquakes. There are two types of modes: spheroidal modes ${}_nS_l$, which involve *P-SV* wave motion, and toroidal modes ${}_nT_l$, which involve *SH* motion. Since we are particularly interested in improving constraints on compressional mantle structure, we will be measuring spheroidal modes. Normal modes only exist for discrete natural frequencies; each mode is characterized by its radial

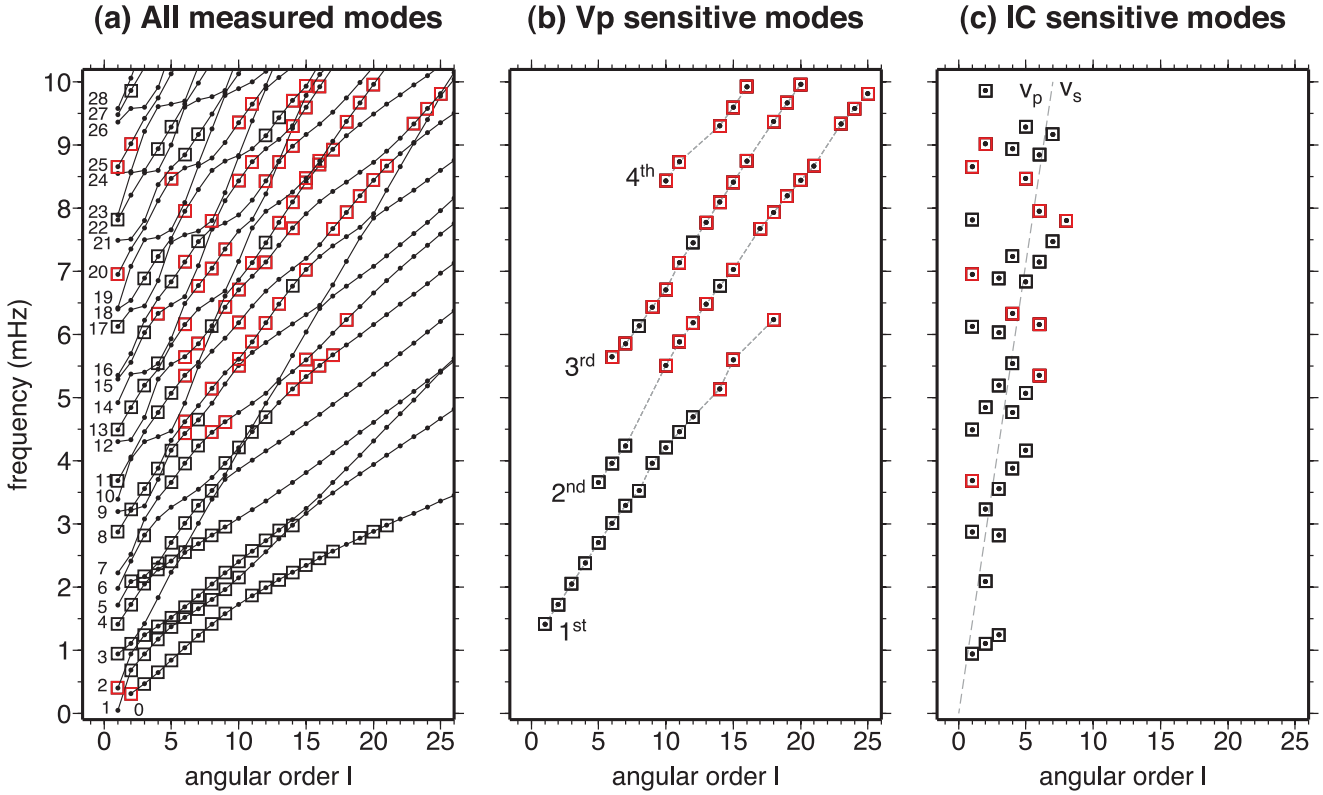

Figure 2. Frequency versus angular order l of the measured modes, (a) all modes measured here, (b) the four 'branches' of modes particularly sensitive to compressional velocity v_p in the mantle and (c) modes sensitive to the inner core. Black squares denote modes measured here, which have been measured before by He & Tromp (1996), Resovsky & Ritzwoller (1998) or Durek & Romanowicz (1999); red squares indicate new modes for which no reported splitting function measurements exist in the literature. The numbers in (a) are the overtone numbers n of each branch; in (b) the compressional wave branches are annotated which cross-cut the overtone branches of (a). The dashed line in (c) denotes the division between modes mainly sensitive to inner-core v_p (on the left) or v_s (on the right).

order or overtone number n and angular order l. For fundamental modes $n = 0$. Modes with $n > 0$ are called overtones. The different branches with constant n can be identified in Fig. 2(a). Modes with low radial order and high angular order are equivalent to laterally propagating waves in the upper mantle (i.e. surface waves). Modes corresponding to steeply travelling waves that are sensitive to the deep mantle and inner core typically have large n and small l (Nolet & Kennett 1987). Frequencies of observed inner-core sensitive modes are shown in Fig. 2(c).

Each spheroidal mode multiplet ${}_nS_l$ consists of $2l + 1$ singlets. In a spherical, non-rotating, elastic, isotropic earth model the normal-mode frequencies of one modal multiplet are degenerate, that is, all $2l + 1$ singlets have the same frequency. The Earth's rotation, ellipticity and the presence of heterogeneity and anisotropy cause splitting, which removes the degeneracy resulting in distinct singlet frequencies. This greatly distorts the amplitude and phase spectra of the multiplets (Dahlen, 1968, 1969; Woodhouse & Dahlen, 1978; Woodhouse, 1980), see Dahlen & Tromp (1998) for an extended overview. The splitting of the longest-period modes is primarily due to rotation and ellipticity of the Earth. Splitting due to heterogeneity and anisotropy is more dominant for shorter period modes.

In the so-called 'self-coupling' approximation, split modes may be treated as isolated and are only sensitive to even-degree structure in the Earth. If two (or more) modes are close in frequency, self-coupling may not be valid and 'cross-coupling' (i.e. resonance) between the two modes needs to be taken into account (e.g. Dahlen & Tromp 1998; Resovsky & Ritzwoller 1998; Deuss & Woodhouse 2001). Here, we will only take cross-coupling into account between strongly coupled modes whose singlets cannot be observed individually. Wide-band coupling (e.g. Deuss & Woodhouse 2001) will be considered here a second-order effect. While direct inversion of spectra is the optimal way to incorporate normal-mode spectra in tomographic inversions (Li *et al.* 1991; Durek & Romanowicz 1999; Kuo & Romanowicz 2002), we argue that a lot can still be learned from splitting function measurements, especially for modes that have not been studied before. Splitting function coefficients are easily used by other researchers and incorporated into their inversion for mantle structure (e.g. for mantle shear wave velocity models S20RTS and S40RTS; Ritsema *et al.* 1999, 2011), which is not the case for normal-mode spectra. In addition, the uncertainties associated with the splitting-function coefficients can be used to evaluate our data and, for example, to investigate the validity of existing mantle models.

The splitting and cross-coupling of single modes or pairs of modes can be described using the generalized splitting function approach (Resovsky & Ritzwoller 1998). Splitting functions were introduced by Woodhouse & Giardini (1985) and the first measurements were published by Woodhouse *et al.* (1986), Ritzwoller *et al.* (1986), Giardini *et al.* (1987), Giardini *et al.* (1988) and Ritzwoller *et al.* (1988). Splitting functions are linearly dependent on the heterogeneous and anisotropic structure in the Earth; they are also used to visualize how a normal mode 'sees' a depth-averaged Earth structure. The splitting function coefficients c_{st} are given by

$$c_{st(kk')} = \int_0^a \delta m_{st}(r) K_{s(kk')}(r) \mathrm{d}r + \sum_d \delta h_{st} H^d_{s(kk')}, \qquad (1)$$

where δm_{st} and δh_{st} are the coefficients of the Earth's heterogeneity (compressional velocity v_p, shear wave velocity v_s and density ρ) and discontinuity topography in terms of spherical harmonics and $K_s(r)$, H_s^d are known kernels (Woodhouse, 1980). s is the angular order and t the azimuthal order of the spherical harmonic used to describe the structure in the Earth. a is the radius of the Earth and k denotes a spheroidal mode with radial and angular order n, l. For self-coupling, $k = k'$ and s is even. Cross-coupling between pairs of normal modes with $k \neq k'$ allows sensitivity to odd-degree structure, if the difference in angular order $l - l'$ between the two normal modes is an odd number. If $l - l'$ is an even number, then the cross-coupling is sensitive to even structure only.

We define the c_{st} coefficients following Masters *et al.* (2000b) and Resovsky & Ritzwoller (1998). They can be converted from the raw coefficients A_{st}, B_{st} (i.e. Woodhouse *et al.* 1986; Giardini *et al.* 1988; He & Tromp, 1996; Durek & Romanowicz, 1999) using

$$c_{st} = (-1)^t (2\pi)^{1/2} (A_{st} - i\,B_{st}) \quad \text{for } t > 0, \tag{2}$$

$$c_{st} = (4\pi)^{1/2} A_{st} \text{ for } t = 0, \tag{3}$$

$$c_{st} = (2\pi)^{1/2} (A_{s|t|} + \mathrm{i} B_{s|t|}) \text{ for } t < 0. \tag{4}$$

$\mathrm{Re}(c_{00})$ and $\mathrm{Im}(c_{00})$ are related to the shift in centre frequency f_c and radial quality factor Q of each mode with respect to the 1-D reference model, using

$$f_c = f_0 + (4\pi)^{-1/2} \mathrm{Re}(c_{00}), \tag{5}$$

$$Q = \frac{f_c}{2\left(\frac{f_o}{2Q_0} + (4\pi)^{-1/2} \mathrm{Im}(c_{00})\right)}, \tag{6}$$

where f is frequency in Hz and f_0 and Q_0 are the frequency and quality factor of the reference model. Splitting coefficients can be visualized by plotting a splitting function map $F(\theta, \phi)$, which is analogous to a phase-velocity map in surface-wave analysis, that is,

$$F(\theta, \phi) = \sum_{s,t} c_{st} Y_s^t(\theta, \phi), \tag{7}$$

where $Y_s^t(\theta, \phi)$ are the complex fully normalized spherical harmonics according to Edmonds (1960).

We use PREM (Dziewonski & Anderson, 1981) as the 1-D reference model. We also compute splitting functions for a model of heterogeneous Earth structure, to compare with our measurements. We use the shear wave velocity model S20RTS (Ritsema *et al.*, 1999) and scaling is of the form $\delta v_p/v_p = \alpha \delta v_s/v_s$ and $\delta\rho/\rho = \beta \delta v_s/v_s$. We use $\alpha = 0.5$ and $\beta = 0.3$. Crustal structure is added in the form of topography, ocean depth and crustal thickness as given in model CRUST5.1 (Mooney *et al.*, 1998).

2.2 Synthetic seismograms

To measure splitting coefficients c_{st}, we need to calculate synthetic seismograms for a given mode (or small group of modes) and the corresponding splitting coefficients. We use a method very similar to Li *et al.* (1991). Synthetic normal-mode seismograms are computed by summation of normal modes, using the method explained in Deuss & Woodhouse (2001). The synthetic seismogram can be written as a harmonic function of time t

$$u(t) = \mathrm{Re}\left[\mathbf{r} \cdot \mathrm{e}^{\mathrm{i}\sqrt{\mathbf{M}}t} \cdot \mathbf{s}\right], \tag{8}$$

where $\mathbf{s}$ is the source vector and depends upon the moment tensor, and $\mathbf{r}$ is the receiver vector and depends upon instrument orientation and incorporates instrumental response. $\mathbf{r}$ and $\mathbf{s}$ are computed for PREM (Dziewonski & Anderson, 1981). $\mathbf{M}$ is the matrix containing the splitting coefficients. Without ellipticity, rotation and aspherical heterogeneity, $\mathbf{M}$ is diagonal and contains only the degenerate multiplet frequencies ω_0^2, where ω_0 is frequency in radians/sec. However, $\mathbf{M}$ is not diagonal when rotation, ellipticity, heterogeneity and anisotropy are taken into account. In that case we have to diagonalize $\mathbf{M}$ to compute its exponential. We do this by using eigenvalue decomposition, that is, $\mathbf{MU} = \mathbf{U}\Lambda$, where the matrix $\mathbf{U}$ contains the eigenvectors and Λ is the diagonal matrix of non-degenerate eigenvalues ω^2. The synthetic seismogram $u(t)$ can then be written as

$$u(t) = \mathrm{Re}\left[(\mathbf{r} \cdot \mathbf{U})\mathrm{e}^{\mathrm{i}\sqrt{\Lambda}t}(\mathbf{U}^{-1} \cdot \mathbf{s})\right]. \tag{9}$$

$\mathbf{M}$ is now a complex matrix that contains the degenerate multiplet frequencies ω_0^2 for PREM and the contributions of Coriolis force, ellipticity and the Earth's internal heterogeneity in terms of the splitting coefficients. In the self-coupling approximation $\mathbf{M}$ is a block diagonal matrix of size $(2l + 1) \times (2l + 1)$, where l is the angular order of the mode. For coupled modes, there will be both block diagonal contributions from every mode and off-diagonal blocks of size $(2l + 1) \times (2l' + 1)$ describing the cross-coupling interactions. For a pair of modes k, k' with degenerate frequencies ω_k,$\omega_{k'}$ in the spherical reference model, we can write $\mathbf{M}$ involving splitting function coefficients c_{st} as follows:

$$\mathbf{M}_{mm'}^{(kk')} = \omega_0^2 \delta_{kk'} + \omega_0 \mathbf{W}_{mm'}^{(kk')} + \sum_{s=l-l'}^{l+l'} \sum_{t=-s}^{s} \gamma_{ll's}^{mm't} c_{st(kk')}, \tag{10}$$

where $\omega_0 = (\omega_k + \omega_{k'})/2$ and $\delta_{kk'} = 0$ if $k \neq k'$ and 1 if $k = k'$. The coefficients $\gamma_{ll's}^{mm't}$ are given by

$$\gamma_{ll's}^{mm't} = \int_0^{2\pi} \int_0^{\pi} Y_l^{m*}(\theta, \phi) Y_s^t(\theta, \phi) Y_l^{m'}(\theta, \phi) \sin\theta \mathrm{d}\theta \mathrm{d}\phi, \tag{11}$$

where Y_l^m are again the fully normalized complex spherical harmonics. Equations for evaluating this integral using Wigner 3-j symbols can be found in Woodhouse (1980) and Dahlen & Tromp (1998). The matrix $\mathbf{W}$ describes the effect of the Coriolis force. Ellipticity is included as an additional degree $s = 2$, $t = 0$ term in the heterogeneity and discontinuity topography coefficients. These equations reduce to well-known self-coupling equations for $k = k'$ (and thus $l = l'$). The matrix $\mathbf{M}$ and the corresponding synthetic seismogram can be computed with use of only the splitting function coefficients c_{st} and without knowledge of the model parameters δm_{st}, δh_{st} and the kernels (eq. 1). Once measured, the kernels can be used to invert the c_{st}'s for tomographic mantle and core structure.

The synthetic seismograms depend non-linearly on the splitting coefficients. To formulate the linearized, iterative inverse problem for c_{st} we require partial derivatives of the seismogram $u(t)$ (eq. 9). The derivatives of the seismogram $u(t)$ with respect to the splitting function coefficients c_{st} are:

$$\frac{\partial u(t)}{\partial c_{st}} = \mathrm{Re}\left[\mathrm{e}^{\mathrm{i}\omega t}\left(\mathbf{r} \cdot \frac{\partial \mathbf{U}}{\partial c_{st}}\right)\left(\mathbf{U}^{-1} \cdot \mathbf{s}\right) + (\mathbf{r} \cdot \mathbf{U})\left(\frac{\partial \mathbf{U}^{-1}}{\partial c_{st}} \cdot \mathbf{s}\right) + (\mathbf{r} \cdot \mathbf{U})\,\mathrm{i}t \frac{\partial \omega}{\partial c_{st}}(\mathbf{U}^{-1} \cdot \mathbf{s})\right] \tag{12}$$

where ω is the diagonal matrix $\omega = \sqrt{\Lambda}$. A perturbation δc_{st} in the splitting function parameters leads to a perturbation $\delta\mathbf{M}$ in the

coupling matrix. We use Rayleigh's principle to find the resulting perturbation $\delta\mathbf{U}$ and $\delta\Lambda$ to the eigenvalues and eigenvectors, which are needed to evaluate eq. (12). This gives for the eigenvalue correction,

$$\delta\omega_n^2 = \delta\Lambda = \mathbf{u}_n^{-1}\delta\mathbf{M}\mathbf{u}_n, \tag{13}$$

where $\mathbf{u}_n$ is a column vector of $\mathbf{U}$ and $\mathbf{u}_n^{-1}$ is a row vector of $\mathbf{U}^{-1}$. The corresponding eigenvector corrections are given by

$$\delta\mathbf{u}_n = \Sigma_{l\neq n}\frac{\mathbf{u}_l^{-1}\delta\mathbf{M}\mathbf{u}_n}{\omega_n^2-\omega_l^2}\mathbf{u}_l, \tag{14}$$

$$\delta\mathbf{u}_n^{-1} = \Sigma_{l\neq n}\frac{\mathbf{u}_n^{-1}\delta\mathbf{M}\mathbf{u}_l}{\omega_n^2-\omega_l^2}\mathbf{u}_l^{-1}, \tag{15}$$

where ω_n represent the diagonal elements of ω. These eigenvector corrections are then substituted in eq. (12) for $\frac{\partial\omega}{\partial c_{st}}$, $\frac{\partial\mathbf{U}}{\partial c_{st}}$ and $\frac{\partial\mathbf{U}^{-1}}{\partial c_{st}}$ to compute the derivatives.

2.3 Inversion technique

The synthetic seismogram $u(t)$ depends non-linearly on the splitting function coefficients c_{st}. Therefore, the splitting function coefficients are measured by iterated damped least squares inversion (Tarantola & Valette, 1982). We solve for c_{st} by the iterative application of the recursion

$$\mathbf{c}^{\mathbf{i+1}} = \mathbf{c}^i + \left(\mathbf{A}_i^T\mathbf{C}_\mathrm{d}^{-1}\mathbf{A}_i + \mathbf{C}_\mathrm{m}^{-1}\right)^{-1} \times \left[\mathbf{A}_i^T\mathbf{C}_\mathrm{d}^{-1}(\mathbf{d}-u(\mathbf{c}^i)) - \mathbf{C}_\mathrm{m}^{-1}(\mathbf{c}^i-\mathbf{c}^0)\right] \tag{16}$$

where $\mathbf{A}_i$ is the matrix of partial derivatives calculated using equation (7),

$$\mathbf{A}_i = \left[\frac{\partial u}{\partial \mathbf{c}}\right]_{\mathbf{c}=\mathbf{c}_{st}^i}, \tag{17}$$

and $\mathbf{c}^i$ is the model vector containing the splitting functions for one mode (or small group of modes) and $\mathbf{c}^0$ is the starting model. $\mathbf{d}$ is the data vector containing the corresponding observed normal-mode spectra, $u(\mathbf{c}^i)$ is the synthetic seismogram vector calculated using equation (9) and $\mathbf{C}_\mathrm{d}$ and $\mathbf{C}_\mathrm{m}$ are the *a priori* data and splitting function covariance matrices. The inversion is run for each of the isolated modes and groups of Table 1 separately. The *posteriori* resolution matrix R can be defined in the neighbourhood of the final model $\mathbf{c}_\infty$,

$$\mathbf{R} = (\mathbf{A}_\infty^T\mathbf{C}_\mathrm{d}^{-1}\mathbf{A}_\infty + \mathbf{C}_\mathrm{m}^{-1})^{-1}\mathbf{A}_\infty^T\mathbf{C}_\mathrm{d}^{-1}\mathbf{A}_\infty. \tag{18}$$

The trace of the resolution matrix then represents the effective number of degrees of freedom of the solution, or the effective number of independent model parameters.

We assume that the data and model covariances $\mathbf{C}_\mathrm{d}$ and $\mathbf{C}_\mathrm{m}$ are the same for all data or model parameters. In this case, equation (16) can be rewritten in such a way that it only depends on $\mathbf{C}_\mathrm{d}/\mathbf{C}_\mathrm{m}$ and we apply damping by using one constant damping parameter $\mathbf{C}_\mathrm{d}/\mathbf{C}_\mathrm{m}$ for all the model and data parameters. The smaller this ratio becomes, the less damping is applied. We vary this ratio by several orders of magnitude and generally find that our results converge to constant values when lowering the damping value, implying that we do not have null space problems and our results are not dependent on the choice of damping parameter. The centre frequency and quality factor of the modes are the most robust parameters in the inversion, and therefore we do not damp these parameters. We estimate the optimal damping by investigating misfit, squared model size and effective number of independent model parameters as a function of the damping parameter and by cross-validation. We did not find any improvement in our results by applying derivative damping, where the model covariance matrix $\mathbf{C}_\mathrm{m}$ is proportional to angular order of the splitting function coefficients s. Thus, our use of a single damping parameter $\mathbf{C}_\mathrm{d}/\mathbf{C}_\mathrm{m}$ is justified.

For all mantle sensitive modes with frequencies below 4 mHz, it suffices to start our inversions from the spherical reference model (PREM, Dziewonski & Anderson 1981), taking only ellipticity and rotation into account. Such treatment prevents the choice of starting model from influencing the results for aspherical structure. For modes with higher frequencies, it is necessary to use a 3-D mantle model (in our case S20RTS, Ritsema *et al.* 1999) as a starting point in our inversion. Even for the modes for which S20RTS is used as a starting model, we find significant reduction in misfit compared to the S20RTS predictions (see Table 2). To measure modes sensitive to the inner core, we tried four different inner-core anisotropy starting models (Woodhouse *et al.* 1986; Tromp 1993; Durek & Romanowicz 1999; Beghein & Trampert 2003), in addition to S20RTS and only PREM. We only report inner-core sensitive modes for which the different starting models give consistent splitting-function measurements. For each inversion we use a range of damping parameters differing by several orders of magnitude. We only include splitting-function measurements for which reduced damping, does not anomalously increase splitting-function

Table 2. Normal-mode spectra used in this study; a total number of 107 504 normal-mode spectra are used in the splitting function inversions. PREM denotes the misfit including only ellipticity and rotation; the misfits for the S20RTS model and after c_{st} measurement are also given. Bold modes correspond to new modes for which splitting functions have not been measured before, stars denote inner-core sensitive modes and 'p' denotes modes sensitive to v_p in the mantle. Modes between brackets were included in the measurement procedure for completeness, but their splitting functions are not constrained well enough by the data to be reported. N_{ev} denotes the number of events and N_s the total number of spectra.

Spectral segment	PREM misfit	S20RTS misfit	c_{st} misfit	N_s	N_{ev}
${}_0\mathbf{S}_2$	0.26	0.26	0.22	78	8
${}_0S_3({}_0T_2-{}_2S_1)$	0.21	0.20	0.18	364	37
${}_0S_4({}_0T_3-{}_1S_2)$	0.26	0.23	0.15	578	56
${}_0S_5$	0.37	0.28	0.11	553	65
${}_0S_6$	0.46	0.36	0.13	1356	82
${}_0S_7$	0.56	0.44	0.16	1733	87
${}_0S_8-{}_4S_1^p({}_0T_9)$	0.58	0.31	0.14	1897	89
${}_0S_9({}_0T_{10})$	0.53	0.32	0.19	1970	91
${}_0S_{11}-{}_2S_7({}_0T_{12})$	0.89	0.72	0.42	846	86
${}_0S_{12}({}_6S_1^*-{}_0T_{13})$	0.64	0.40	0.30	1484	91
${}_0S_{13}({}_0T_{14})$	0.67	0.38	0.29	2507	91
${}_0S_{14}-{}_2S_9({}_0T_{15})$	0.79	0.47	0.27	2631	91
${}_0S_{15}({}_0T_{16})$	0.77	0.41	0.29	2663	91
${}_0S_{16}({}_0T_{17})$	0.79	0.39	0.29	2552	91
${}_0S_{17}-{}_2S_{11}({}_0T_{18})$	0.89	0.52	0.33	2402	91
${}_0S_{19}({}_0T_{20})$	0.97	0.84	0.49	1227	90
${}_0S_{20}({}_8S_1^*-{}_0T_{21})$	0.89	0.53	0.47	2255	89
${}_0S_{21}-{}_1S_{14}({}_0T_{22})$	0.93	0.42	0.31	2872	91
${}_1S_2({}_0S_4-{}_0T_3)$	0.23	0.23	0.18	136	9
${}_1S_3-{}_3S_1^*$	0.27	0.38	0.15	468	54
${}_1S_4$	0.28	0.31	0.19	1046	77
${}_1S_5-{}_2S_4$	0.52	0.39	0.15	1464	84
${}_1S_6-{}_2S_5$	0.84	0.74	0.17	1335	82
${}_1S_7$	0.69	0.25	0.16	1244	74
${}_1S_8$	0.94	0.43	0.15	1469	75
${}_1S_9$	1.01	0.63	0.18	948	74

Table 2. (*Continued.*)

Spectral segment	PREM	S20RTS	c_{st}	N_s	N_{ev}
${}_1S_{10}$	1.02	0.79	0.27	780	70
${}_2\mathbf{S}_1$	0.60	0.65	0.48	32	2
${}_2S_3^*$	1.21	1.14	0.36	503	62
${}_2S_6$	0.53	0.26	0.16	1192	84
${}_2S_8$–${}_4S_3^p$	0.80	0.39	0.18	2634	91
${}_2S_{10}$–${}_4S_5$	1.09	0.46	0.19	2428	89
${}_2S_{12}$	1.04	0.37	0.19	2668	90
${}_2S_{13}$	0.94	0.48	0.34	1804	90
${}_3S_2^*$	2.03	1.84	0.13	224	26
${}_3S_6$	0.86	0.73	0.67	1240	87
${}_3S_7$–${}_5S_5^p$	0.57	0.64	0.21	1902	86
${}_3S_8$–${}_6S_3^*$	0.80	0.53	0.18	1734	89
${}_3S_9$	0.94	0.72	0.57	1936	90
${}_4S_2^p(-{}_0S_{10}-{}_0T_{11})$	0.61	0.41	0.30	1538	90
${}_4S_4(-{}_1T_8)$	0.49	0.30	0.21	1203	86
${}_5S_2^*(-{}_0S_{13}-{}_0T_{14})$	0.61	0.50	0.47	999	81
${}_5S_3$	0.40	0.19	0.17	1189	86
${}_5S_4^p(-{}_2T_4)$	0.50	0.45	0.21	1779	89
${}_5S_6^p(-{}_0S_{21}-{}_0T_{22})$	0.71	0.75	0.38	979	86
${}_5S_7^p$	0.87	1.03	0.39	1491	78
${}_5S_8^p$	0.99	1.04	0.39	1738	85
${}_5S_{11}^p$–${}_7\mathbf{S}_8$	1.22	1.27	0.51	376	73
${}_5S_{12}^p$	0.74	1.40	0.44	478	63
$\mathbf{{}_5S_{14}^p}$–${}_9\mathbf{S}_8$	1.44	1.23	0.29	1102	79
$\mathbf{{}_5S_{15}^p}$–$\mathbf{{}_{11}S_6^*}$	1.47	1.03	0.32	1061	73
${}_5\mathbf{S}_{16}$–$\mathbf{{}_8S_{10}^p}$	1.74	0.93	0.34	1114	80
${}_5\mathbf{S}_{17}$	1.35	0.64	0.38	715	65
${}_6S_9^p$–${}_7S_6^p$	1.35	0.93	0.34	1760	87
${}_6S_{10}^p$	1.31	1.80	0.36	1179	75
$\mathbf{{}_6S_{15}^p}$–${}_9\mathbf{S}_{10}$	1.16	0.78	0.43	441	62
$\mathbf{{}_6S_{18}^p}$	1.26	1.11	0.42	798	78
${}_7S_5^p$	1.29	0.66	0.39	1444	88
${}_7S_7^p$	1.82	1.07	0.26	905	77
${}_7\mathbf{S}_9$–${}_9\mathbf{S}_6$	1.07	0.82	0.61	351	57
${}_8S_1^*(-{}_0S_{20}-{}_0T_{21})$	0.85	0.67	0.24	594	60
${}_8S_5^*(-\mathbf{{}_5S_{10}^{J*}})$	1.29	1.28	0.31	1078	75
${}_8\mathbf{S}_6$	2.33	1.53	0.49	599	56
${}_8S_7$	1.95	0.52	0.30	350	59
${}_9S_2^*$	0.77	0.77	0.35	574	54
${}_9S_3^*$	1.26	0.92	0.40	408	61
${}_9S_4^*$	1.22	0.88	0.45	418	57
$\mathbf{{}_9S_{11}^p}$	1.70	0.55	0.39	885	72
$\mathbf{{}_9S_{12}^p}$–${}_{10}\mathbf{S}_{10}$	1.44	0.53	0.28	704	66
$\mathbf{{}_9S_{13}^p}(-{}_5\mathbf{S}_{22})$	1.57	0.69	0.29	588	58
${}_9S_{14}^p$–${}_{14}\mathbf{S}_7$	1.57	0.70	0.33	573	49
$\mathbf{{}_9S_{15}^p}$–${}_{14}\mathbf{S}_8$	1.62	1.02	0.48	340	39
$\mathbf{{}_{10}S_{17}^p}$–${}_{11}\mathbf{S}_{14}(-\mathbf{{}_{19}S_5^*})$	1.67	0.69	0.32	388	46
$\mathbf{{}_{10}S_{18}^p}$–$\mathbf{{}_{18}S_6^*}$	1.56	1.01	0.43	253	29
$\mathbf{{}_{10}S_{19}^p}(-\mathbf{{}_{22}S_2^*})$	1.76	1.58	0.40	351	31
$\mathbf{{}_{10}S_{20}^p}$–${}_{15}\mathbf{S}_{12}$–$\mathbf{{}_{16}S_{10}^p}$	2.62	1.26	0.27	749	57
$\mathbf{{}_{10}S_{21}^p}$–${}_{12}\mathbf{S}_{16}$–$\mathbf{{}_{25}S_1^*}$	1.42	1.34	0.45	575	36
$\mathbf{{}_{11}S_1^*}(-\mathbf{{}_8S_4^{J*}})$	3.10	2.51	0.45	107	17
${}_{11}S_4^*$	1.85	1.54	0.29	654	51
${}_{11}S_5^*$	1.70	0.70	0.28	757	60
$\mathbf{{}_{11}S_9^p}$	2.18	1.15	0.38	462	40
$\mathbf{{}_{11}S_{10}^p}(-{}_4\mathbf{S}_{28})$	1.87	1.40	0.43	238	42
${}_{11}\mathbf{S}_{12}$–$\mathbf{{}_{12}S_{11}^p}$–${}_{16}S_6^*$	2.16	1.30	0.34	844	73

Table 2. (*Continued.*)

Spectral segment	PREM	S20RTS	c_{st}	N_s	N_{ev}
$\mathbf{{}_{11}S_{23}^p}$–$\mathbf{{}_{13}S_{18}^p}$–${}_{19}\mathbf{S}_{10}$	2.20	1.55	0.32	675	50
$\mathbf{{}_{11}S_{24}^p}$–$\mathbf{{}_{15}S_{15}^p}$	1.89	1.08	0.33	426	42
$\mathbf{{}_{11}S_{25}^p}$	1.30	1.22	0.60	247	35
$\mathbf{{}_{12}S_6^p}$	1.50	0.86	0.60	230	36
$\mathbf{{}_{12}S_7^p}$	1.42	0.80	0.46	455	56
${}_{12}S_8^p$–${}_{17}S_1^*$	2.24	1.37	0.27	779	61
${}_{12}S_{12}^p$–${}_{16}S_7^*$	2.59	1.54	0.31	891	67
$\mathbf{{}_{12}S_{13}^p}$	1.81	1.61	0.41	512	49
$\mathbf{{}_{12}S_{14}^p}$	1.72	1.79	0.45	285	42
$\mathbf{{}_{12}S_{15}^p}$	1.92	1.51	0.39	475	41
${}_{12}\mathbf{S}_{17}$–${}_{23}S_4^*$	2.31	1.57	0.35	425	38
${}_{13}S_1^*$	2.90	2.62	0.31	440	29
${}_{13}S_2^*$	1.95	0.86	0.16	596	30
${}_{13}S_3^*$	1.81	1.05	0.34	362	32
$\mathbf{{}_{13}S_6^*}$	2.38	0.93	0.39	313	43
${}_{13}\mathbf{S}_{15}$–$\mathbf{{}_{20}S_5^*}$	2.37	2.30	0.35	330	37
$\mathbf{{}_{13}S_{16}^p}$–${}_{14}\mathbf{S}_{13}$–$\mathbf{{}_{16}S_{11}^p}$	2.33	1.84	0.39	496	50
$\mathbf{{}_{13}S_{19}^p}$–${}_{19}\mathbf{S}_{11}$	1.71	1.32	0.39	463	43
$\mathbf{{}_{13}S_{20}^p}$	1.59	0.85	0.37	382	39
${}_{14}S_4^*(-\mathbf{{}_{11}S_7^*})$	1.77	1.31	0.43	435	32
${}_{14}\mathbf{S}_9(-\mathbf{{}_{20}S_2^*})$	1.84	2.14	0.36	383	57
${}_{14}\mathbf{S}_{14}$	1.01	0.61	0.34	127	26
${}_{15}S_3^*$	1.49	1.06	0.35	426	49
$\mathbf{{}_{15}S_4^*}$	1.26	1.27	0.52	141	29
$\mathbf{{}_{15}S_{16}^p}$–${}_{17}\mathbf{S}_{15}$	1.76	1.24	0.43	521	49
${}_{16}S_5^*(-\mathbf{{}_{17}S_4^{J*}})$	2.21	1.62	0.31	515	41
$\mathbf{{}_{16}S_{14}^p}$–${}_{23}S_5^*$	1.65	1.11	0.29	569	44
$\mathbf{{}_{17}S_8^*}$–${}_{22}S_1^*$	1.17	1.37	0.34	346	27
${}_{17}S_{12}$–${}_{21}S_7^*$	2.60	1.25	0.30	387	37
${}_{17}S_{13}(-\mathbf{{}_{25}S_3^*})$	2.00	1.64	0.32	514	47
${}_{17}\mathbf{S}_{14}$	1.84	2.08	0.41	165	29
${}_{18}S_3^*$	2.34	2.68	0.45	285	35
${}_{18}S_4^*$	1.58	1.10	0.27	594	41
$\mathbf{{}_{20}S_1^*}$	1.00	0.52	0.34	138	17
${}_{21}S_6^*$	3.17	1.72	0.35	293	32
$\mathbf{{}_{25}S_2^*}$	1.33	1.58	0.50	384	36
${}_{27}S_2^*$	1.60	1.67	0.32	259	21

coefficients. Ideally, lowering the damping leads to convergence to constant splitting-function measurements.

To determine error values for our measurements, we used cross-validation to remeasure the splitting coefficients, leaving out different events in different runs. This procedure allows us to assess the importance of the large earthquakes, such as the 1994 Bolivia event and the 2004 Sumatra event, on the final results, as each one will be left out completely in different cross-validation runs. The maximum spread in the range of the cross-validation measurements for each measured splitting function coefficient is then used to estimate the size of the error for that coefficient. This is a conservative estimate of the error in our measurements.

3 DATA

We have selected normal-mode spectra for 91 large events since 1976 with $M_w \geq 7.4$ (Fig. 1 and Table 1), which is a significant

expansion of data sets used in other studies. For example, He & Tromp (1996) used only two events, the Bolivia and Kuril Islands events of 1994, to measure splitting functions. Resovsky & Ritzwoller (1998) analysed a total of 33 events from 1977 to 1995. Our data set includes spectra from seven earthquakes in continental regions, including the 2008 Wenchuan, China event ($M_w = 7.9$), the 1999 Turkey event ($M_w = 7.6$), and the 2005 Pakistan event ($M_w = 7.6$) and 21 subduction zone events deeper than 100 km depth, which are useful for measuring overtones. We have also included some events with magnitude 7.4, but these are always deeper than 100 km. Shallow events with such low magnitudes do not produce spectra with high enough signal-to-noise ratio. For each earthquake we obtained up to a week of waveform data from the IRIS data centre. We do not use events which have other events of similar magnitude appearing within a week from the main event. Glitches and smaller magnitude events are removed manually, which significantly lowers the signal-to-noise ratio in the spectra. The tidal signal is removed by fitting sine curves with the tidal frequencies and removing the corresponding long-period signal from the time-series.

Fig. 3 shows two example spectra, one for the large amplitude Northern Sumatra event with a depth of 25.8 km, and the other one for the much smaller magnitude $M_w = 7.4$ event at Vanuatu with a depth of 141.1 km. The Sumatra event has a large signal-to-noise ratio, and clear modal peaks can even observed even below 1 mHz. Because this event is shallow, the fundamental mods between about 1 and 3.5 mHz have the strongest amplitudes. The smaller event at Vanuatu has a much smaller signal-to-noise ratio and we are only able to observe clear modal peaks for frequencies larger than 1.5 mHz. Because this is a deeper event, the modal peaks have larger relative amplitudes above 3.5 mHz than is seen in the larger event. This is because the deeper event excites more overtones, which become observable at larger frequencies.

We only use vertical component data, as we are interested in spheroidal modes whose main energy is on the vertical component of the seismogram. The spectra are derived from several tens of hours of seismogram to calculate spectra, which are roughly of the length of 1 Q-cycle per mode (Dahlen, 1982). The Q-cycle of a mode is defined as the quality factor Q of a mode multiplied by its period T in seconds, and is the time required for the modal signal to decay to $e^{-\pi}$. The first several hours of each seismogram are not used, as the body waves in this part of the signal lead to noise and interfere in the spectra. Sometimes up to 10 or 15 hours are removed, especially for the higher-order overtones, to remove the fundamental modes and other modes with shorter Q-cycles that will

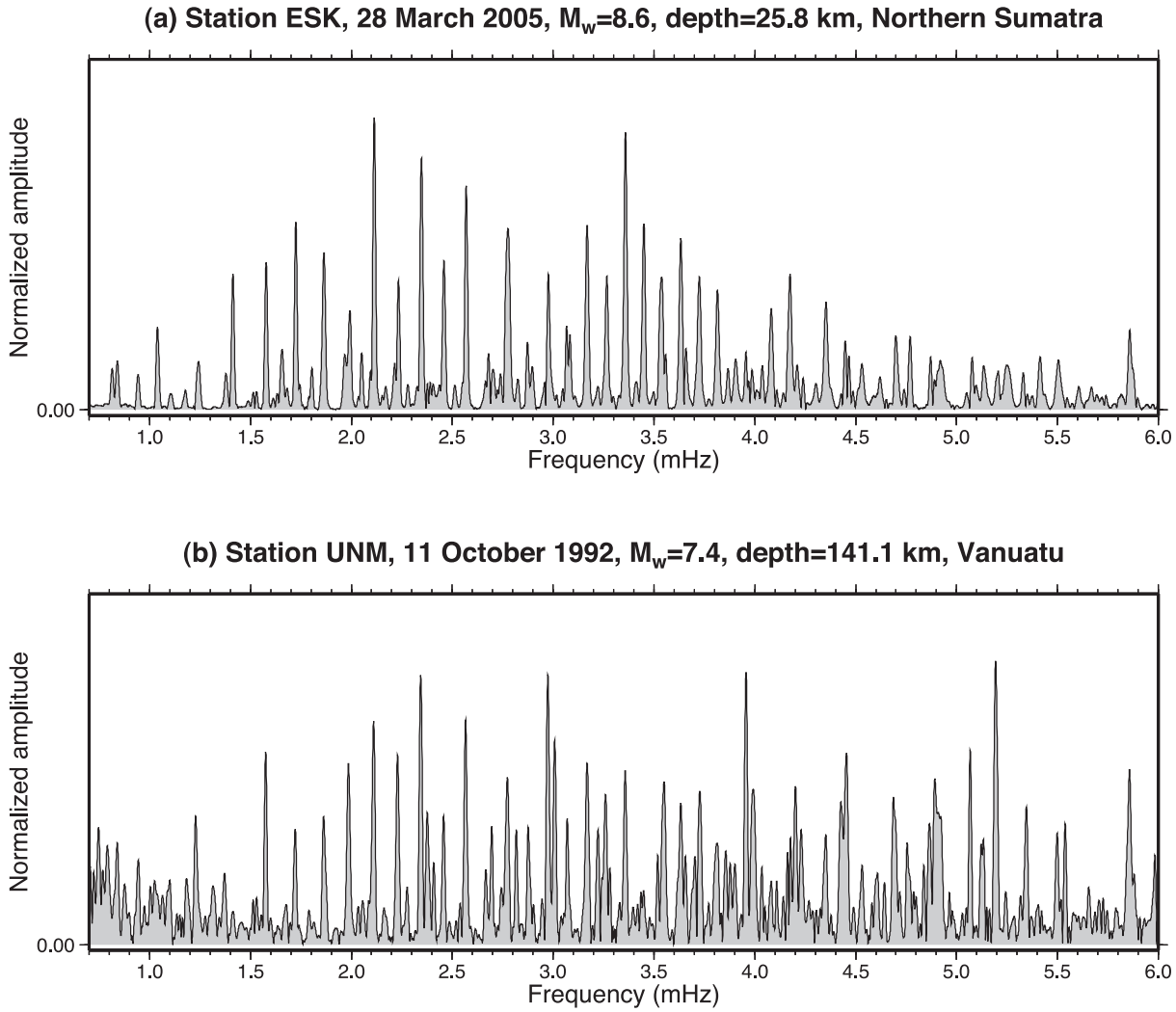

Figure 3. Observed spectra for time series of 5–40 hr length, for (a) the large magnitude $M_w = 8.8$ Northern Sumatra event of 2005 and (b) the much smaller magnitude $M_w = 7.4$ Vanuatu event of 1992.

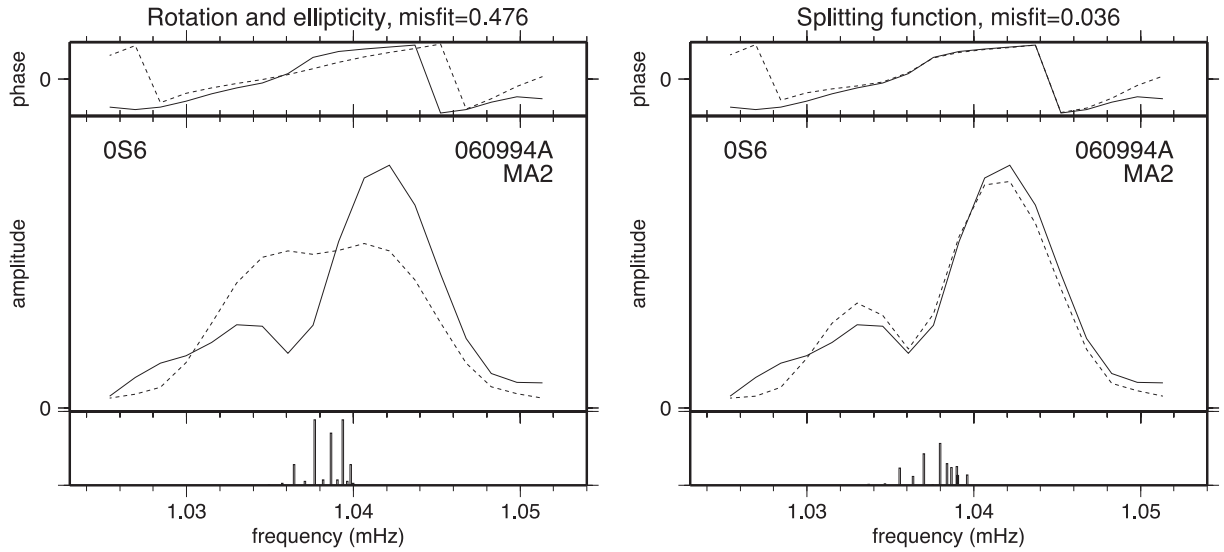

Figure 4. Example of a spectral window for mode ${}_0S_6$. (a) Observed data (solid line) and synthetic spectrum (dashed line) using only rotation and ellipticity (misfit =0.476). (b) Synthetic spectrum (dashed line) using our measured splitting function in addition to rotation and ellipticity, showing a much improved fit (misfit = 0.036) with the observed data (solid line). Vertical bars denote the synthetic singlet frequencies.

have attenuated after the first few hours. The time-series are padded with zeroes and Fourier transformed to the frequency domain. The synthetic seismograms are processed in exactly the same way as the real data.

The spectrum up to 10 mHz consists of a large number of toroidal and spheroidal modes. Many appear in clusters, but a significant number of modes are sufficiently isolated from other modes so that the self-coupling or group-coupling approximation can be applied. We make an initial selection of individual spectra for each mode or small group of modes for which the signal-to-noise ratio is larger than two. The signal is defined as the maximum peak of the mode, and the noise is defined as the maximum amplitude in parts of the spectra just next to the target mode where no other modes are predicted to exist. We run an inversion for this initial selection of spectra, an then reselect the spectra and remove all outliers which cannot be fit by the splitting-functions measurements. We then run a second inversion for this new data selection, to obtain our final splitting function measurements. For modes with frequency less than 1 mHz we visually inspected all spectra and we kept some records with signal-to-noise ratio of 1.5 and larger, if the spectra looked acceptable.

In total, we measure 196 splitting functions, of which 164 are self-coupled and 32 are cross-coupled splitting functions, and 92 are new measurements. Table 2 shows the list of isolated modes and groups of modes which we measured, including the number of events and total number of spectra used for each inversion. A total of 107 504 spectra have been measured, which is an order of magnitude larger than the number of spectra in previous studies. The majority of our new modes are mantle (and outer core) sensitive modes, totalling 60 newly measured mantle sensitive modes: modes sensitive to v_p are labelled with 'p'. Inner-core sensitive modes are labelled with a star; we have added 10 new measurements of inner-core sensitive modes to previous collections (He & Tromp 1996; Durek & Romanowicz 1999).

We define misfit as the difference between the data $\mathbf{d}_i$ and synthetics $\mathbf{u}_i(c_{st})$, normalized by the norm of the data, that is,

$$\text{misfit} = \frac{1}{N}\sum^{N}\frac{\sum_{i=1}^{n}(\mathbf{d}_i - \mathbf{u}_i(c_{st}))^2}{\sum_{i=1}^{n}(\mathbf{d}_i)^2}, \qquad (19)$$

where n are the number of data points in each spectral segment and N are the total number of spectral segments for a specific mode. We take into account both amplitude and phase in calculating the misfit. Table 2 shows the misfit for each mode with respect to the PREM model, including only splitting due to ellipticity and rotation. Also shown is the S20RTS + CRUST5.1 misfit and the misfit including our new splitting function measurements. The PREM misfit is smaller than 1 for the longest period normal modes, and only modest improvement is obtained when adding our splitting function measurements. This is to be expected, as splitting of the longest period normal modes is dominated by ellipticity and rotation. For the shorter period normal modes, the PREM misfit is larger than 1. Since these modes are strongly sensitive to mantle heterogeneity, a significant reduction in misfit is obtained when our splitting function measurements are incorporated in synthetic spectra. Fig. 4 shows an observed spectral window for mode ${}_0S_6$ and illustrates the improvement in misfit between data and synthetic when including our splitting function measurement as compared to using PREM and splitting due to ellipticity and rotation only.

4 SPLITTING FUNCTION OBSERVATIONS

4.1 Mantle sensitive modes

4.1.1 Comparison with previous measurements

Table 3 shows the centre frequency and Q of all our measured splitting functions; for completeness we have also included the long-period modes, which were already discussed by Deuss *et al.* (2011). Tables with all even-degree self-coupling splitting-function coefficients and even- and odd-degree cross-coupling coefficients can be found in additional online material to this paper and also online at http://bullard.esc.cam.ac.uk/~deuss/research/splitting-functions/.

Most modes below 3 mHz have been measured before by Resovsky & Ritzwoller (1998), and our results show very similar splitting function coefficients for a large number of modes, especially at low angular order. However, our data set is significantly larger, so we have been able to measure the splitting function

Table 3. Centre frequencies in μHz and quality factors Q for the modes measured in this study. New modes are in bold, inner-core sensitive modes are denoted by a star and mantle v_p sensitive modes are labelled with a 'p'.

Mode	PREM f_0	Measured f_c	PREM Q_0	Measured Q
$_0\mathbf{S}_2$	309.28	309.48 ± 0.02	510	477 ± 177
$_0S_3$	468.56	468.46 ± 0.04	418	405 ± 14
$_0S_4$	647.08	646.78 ± 0.03	373	373 ± 9
$_0S_5$	840.44	839.99 ± 0.04	356	364 ± 5
$_0S_6$	1038.23	1037.54 ± 0.04	347	358 ± 4
$_0S_7$	1231.81	1230.98 ± 0.03	342	350 ± 3
$_0S_8$	1413.53	1412.81 ± 0.02	337	342 ± 2
$_0S_9$	1578.30	1577.56 ± 0.02	333	330 ± 2
$_0S_{11}$	1862.43	1861.90 ± 0.08	322	294 ± 4
$_0S_{12}$	1990.39	1989.73 ± 0.03	315	295 ± 3
$_0S_{13}$	2112.95	2112.02 ± 0.04	307	294 ± 3
$_0S_{14}$	2231.41	2230.47 ± 0.04	298	294 ± 2
$_0S_{15}$	2346.40	2345.45 ± 0.06	289	285 ± 3
$_0S_{16}$	2458.23	2457.50 ± 0.03	279	274 ± 2
$_0S_{17}$	2567.13	2566.53 ± 0.05	269	262 ± 2
$_0S_{19}$	2776.99	2776.86 ± 0.10	250	256 ± 2
$_0S_{20}$	2878.38	2878.36 ± 0.16	241	238 ± 4
$_0S_{21}$	2977.73	2977.48 ± 0.61	232	239 ± 3
$_1S_2$	679.86	679.91 ± 0.05	310	327 ± 5
$_1S_3$	939.83	939.98 ± 0.06	283	303 ± 5
$_1S_4$	1172.85	1172.89 ± 0.05	271	298 ± 3
$_1S_5$	1370.27	1370.09 ± 0.03	292	331 ± 3
$_1S_6$	1522.04	1521.48 ± 0.04	346	400 ± 5
$_1S_7$	1655.52	1654.56 ± 0.06	372	416 ± 5
$_1S_8$	1799.31	1797.86 ± 0.03	379	422 ± 3
$_1S_9$	1963.76	1961.94 ± 0.03	380	420 ± 8
$_1S_{10}$	2148.45	2146.30 ± 0.14	378	426 ± 5
$_1S_{14}$	2975.83	2973.36 ± 0.75	293	291 ± 9
$_2\mathbf{S}_1$	403.95	404.17 ± 0.04	397	414 ± 70
$_2S_3^*$	1242.19	1242.82 ± 0.04	416	450 ± 8
$_2S_4$	1379.19	1379.51 ± 0.03	380	388 ± 2
$_2S_5$	1514.93	1515.23 ± 0.03	302	313 ± 2
$_2S_6$	1680.84	1681.10 ± 0.06	238	236 ± 1
$_2S_7$	1864.96	1865.11 ± 0.05	212	228 ± 4
$_2S_8$	2049.21	2049.39 ± 0.03	198	202 ± 2
$_2S_9$	2228.75	2228.57 ± 0.15	188	186 ± 2
$_2S_{10}$	2402.93	2403.09 ± 0.01	181	186 ± 2
$_2S_{11}$	2572.15	2572.24 ± 0.18	176	178 ± 2
$_2S_{12}$	2737.31	2737.15 ± 0.02	173	175 ± 2
$_2S_{13}$	2899.89	2899.78 ± 0.04	174	175 ± 2
$_3S_1^*$	943.94	944.29 ± 0.04	820	874 ± 34
$_3S_2^*$	1106.21	1106.28 ± 0.10	367	324 ± 3
$_3S_6$	2549.64	2548.80 ± 0.08	276	296 ± 8
$_3S_7$	2686.33	2685.78 ± 0.21	269	283 ± 7
$_3S_8$	2819.64	2819.25 ± 0.03	264	275 ± 2
$_3S_9$	2951.59	2951.39 ± 0.03	259	260 ± 4
$_4S_1^p$	1412.63	1411.80 ± 0.05	355	380 ± 12
$_4S_2^p$	1722.30	1721.41 ± 0.05	434	485 ± 18
$_4S_3^p$	2048.96	2048.27 ± 0.01	480	520 ± 7
$_4S_4$	2279.60	2278.30 ± 0.03	290	292 ± 3
$_4S_5$	2411.43	2411.12 ± 0.03	282	287 ± 5

Table 3. (*Continued.*)

Mode	PREM f_0	Measured f_c	PREM Q_0	Measured Q
$_5S_2^*$	2091.27	2090.47 ± 0.06	318	358 ± 7
$_5S_3$	2169.66	2168.68 ± 0.06	292	310 ± 5
$_5S_4^p$	2379.52	2379.18 ± 0.04	489	531 ± 7
$_5S_5^p$	2703.35	2703.39 ± 0.01	502	568 ± 5
$_5S_6^p$	3010.69	3011.03 ± 0.05	506	547 ± 7
$_5S_7^p$	3290.76	3291.63 ± 0.04	493	579 ± 13
$_5S_8^p$	3525.65	3525.91 ± 0.02	418	463 ± 4
$_5S_{11}^p$	4456.55	4456.84 ± 0.11	375	399 ± 6
$_5S_{12}^p$	4695.98	4695.73 ± 0.03	386	443 ± 4
$_5\mathbf{S}_{14}^\mathbf{p}$	5136.82	5134.93 ± 0.06	372	403 ± 3
$_5\mathbf{S}_{15}^\mathbf{p}$	5330.12	5326.85 ± 0.02	346	365 ± 2
$_5\mathbf{S}_{16}$	5506.97	5502.43 ± 0.10	321	324 ± 2
$_5\mathbf{S}_{17}$	5673.70	5668.75 ± 0.06	304	315 ± 3
$_6S_3^*$	2821.72	2821.70 ± 0.03	426	459 ± 8
$_6S_9^p$	3965.34	3964.99 ± 0.04	321	320 ± 3
$_6S_{10}^p$	4210.76	4211.02 ± 0.03	354	376 ± 2
$_6\mathbf{S}_{15}^\mathbf{p}$	5602.51	5601.23 ± 0.13	272	289 ± 3
$_6\mathbf{S}_{18}^\mathbf{p}$	6235.59	6235.66 ± 0.08	309	327 ± 2
$_7S_5^p$	3659.75	3657.54 ± 0.02	477	514 ± 5
$_7S_6^p$	3958.73	3955.63 ± 0.02	504	557 ± 3
$_7S_7^p$	4237.86	4234.38 ± 0.03	415	446 ± 2
$_7\mathbf{S}_8$	4452.59	4449.42 ± 0.13	322	381 ± 5
$_7\mathbf{S}_9$	4617.94	4614.45 ± 0.14	282	333 ± 4
$_8S_1^*$	2873.36	2872.63 ± 0.01	930	1000 ± 15
$_8S_5^*$	4166.20	4165.22 ± 0.08	612	759 ± 13
$_8\mathbf{S}_6$	4435.23	4430.29 ± 0.03	441	402 ± 3
$_8S_7$	4650.44	4646.44 ± 0.16	352	332 ± 10
$_8\mathbf{S}_{10}^\mathbf{p}$	5508.74	5503.01 ± 0.04	492	489 ± 3
$_9S_2^*$	3231.73	3230.92 ± 0.08	408	439 ± 11
$_9S_3^*$	3554.98	3555.70 ± 0.04	778	742 ± 12
$_9S_4^*$	3877.96	3878.30 ± 0.10	515	521 ± 8
$_9\mathbf{S}_6$	4620.88	4618.88 ± 0.17	331	349 ± 7
$_9\mathbf{S}_8$	5144.46	5138.47 ± 0.06	472	494 ± 4
$_9\mathbf{S}_{10}$	5610.94	5606.09 ± 0.23	320	323 ± 5
$_9\mathbf{S}_{11}^\mathbf{p}$	5885.78	5882.36 ± 0.05	414	391 ± 3
$_9\mathbf{S}_{12}^\mathbf{p}$	6187.26	6183.66 ± 0.04	465	448 ± 4
$_9\mathbf{S}_{13}^\mathbf{p}$	6483.50	6480.68 ± 0.05	485	503 ± 3
$_9S_{14}^p$	6768.24	6764.71 ± 0.03	485	499 ± 5
$_9\mathbf{S}_{15}^\mathbf{p}$	7029.81	7025.29 ± 0.10	430	436 ± 5
$_{10}\mathbf{S}_{10}$	6190.90	6186.47 ± 0.21	376	340 ± 7
$_{10}\mathbf{S}_{17}^\mathbf{p}$	7675.88	7672.66 ± 0.07	388	381 ± 5
$_{10}\mathbf{S}_{18}^\mathbf{p}$	7938.47	7936.38 ± 0.11	411	415 ± 6
$_{10}\mathbf{S}_{19}^\mathbf{p}$	8197.94	8196.75 ± 0.09	412	413 ± 2
$_{10}\mathbf{S}_{20}^\mathbf{p}$	8446.63	8446.05 ± 0.16	391	389 ± 3
$_{10}\mathbf{S}_{21}^\mathbf{p}$	8673.46	8671.33 ± 0.18	342	333 ± 2
$_{11}\mathbf{S}_1^*$	3685.49	3687.69 ± 0.59	664	581 ± 20
$_{11}S_4^*$	4766.87	4765.98 ± 0.09	702	696 ± 11
$_{11}S_5^*$	5074.41	5072.76 ± 0.04	666	642 ± 7
$_{11}\mathbf{S}_{6^*}$	5351.70	5348.93 ± 0.04	463	399 ± 7
$_{11}\mathbf{S}_9^\mathbf{p}$	6437.11	6431.87 ± 0.05	627	614 ± 9
$_{11}\mathbf{S}_{10}^\mathbf{p}$	6712.40	6705.57 ± 0.11	426	431 ± 5
$_{11}\mathbf{S}_{12}$	7149.62	7142.97 ± 0.41	367	372 ± 8
$_{11}\mathbf{S}_{14}$	7686.83	7679.55 ± 0.52	399	361 ± 13

Table 3. (*Continued.*)

Mode	PREM f_0	Measured f_c	PREM Q_0	Measured Q
$_{11}\mathbf{S}^{\mathbf{p}}_{\mathbf{23}}$	9341.09	9332.85 ± 0.25	349	320 ± 4
$_{11}\mathbf{S}^{\mathbf{p}}_{\mathbf{24}}$	9578.37	9570.47 ± 0.24	363	360 ± 3
$_{11}\mathbf{S}^{\mathbf{p}}_{\mathbf{25}}$	9814.24	9808.51 ± 0.13	361	373 ± 8
$_{12}\mathbf{S}^{\mathbf{p}}_{\mathbf{6}}$	5646.54	5643.85 ± 0.15	267	262 ± 6
$_{12}\mathbf{S}^{\mathbf{p}}_{\mathbf{7}}$	5855.87	5852.44 ± 0.10	424	409 ± 4
$_{12}S^{p}_{8}$	6137.16	6132.06 ± 0.06	567	559 ± 5
$_{12}\mathbf{S}^{\mathbf{p}}_{\mathbf{11}}$	7138.83	7133.44 ± 0.04	511	508 ± 6
$_{12}S^{p}_{12}$	7455.08	7448.91 ± 0.04	570	557 ± 3
$_{12}\mathbf{S}^{\mathbf{p}}_{\mathbf{13}}$	7776.99	7769.84 ± 0.11	569	552 ± 3
$_{12}\mathbf{S}^{\mathbf{p}}_{\mathbf{14}}$	8097.36	8090.28 ± 0.09	523	515 ± 9
$_{12}\mathbf{S}^{\mathbf{p}}_{\mathbf{15}}$	8411.27	8404.52 ± 0.09	543	528 ± 5
$_{12}\mathbf{S}_{16}$	8691.80	8686.69 ± 0.11	449	425 ± 7
$_{12}\mathbf{S}_{17}$	8933.92	8928.22 ± 0.14	383	370 ± 10
$_{13}S^{*}_{1}$	4495.73	4494.38 ± 0.08	735	663 ± 5
$_{13}S^{*}_{2}$	4845.26	4844.55 ± 0.02	879	928 ± 8
$_{13}S^{*}_{3}$	5193.82	5193.81 ± 0.10	909	921 ± 13
$_{13}\mathbf{S}^{*}_{\mathbf{6}}$	6161.19	6158.11 ± 0.11	649	570 ± 9
$_{13}\mathbf{S}_{15}$	8474.44	8472.67 ± 0.63	337	337 ± 32
$_{13}\mathbf{S}^{\mathbf{p}}_{\mathbf{16}}$	8752.26	8744.85 ± 0.28	432	388 ± 3
$_{13}\mathbf{S}^{\mathbf{p}}_{\mathbf{18}}$	9371.79	9363.72 ± 0.11	491	490 ± 3
$_{13}\mathbf{S}^{\mathbf{p}}_{\mathbf{19}}$	9671.80	9664.48 ± 0.14	487	501 ± 4
$_{13}\mathbf{S}^{\mathbf{p}}_{\mathbf{20}}$	9961.01	9954.47 ± 0.10	473	478 ± 4
$_{14}S^{*}_{4}$	5541.84	5542.04 ± 0.28	743	693 ± 14
$_{14}\mathbf{S}_{7}$	6772.89	6769.37 ± 0.24	330	324 ± 4
$_{14}\mathbf{S}_{8}$	7047.91	7042.54 ± 0.28	483	416 ± 6
$_{14}\mathbf{S}_{9}$	7354.10	7344.53 ± 0.12	528	545 ± 4
$_{14}\mathbf{S}_{13}$	8734.79	8729.83 ± 0.07	477	474 ± 5
$_{14}\mathbf{S}_{14}$	8985.11	8981.50 ± 0.08	331	368 ± 6
$_{15}S^{*}_{3}$	6035.23	6030.90 ± 0.07	806	764 ± 14
$_{15}\mathbf{S}^{*}_{\mathbf{4}}$	6332.34	6323.45 ± 0.20	399	405 ± 7
$_{15}\mathbf{S}_{12}$	8432.74	8427.74 ± 0.13	572	553 ± 9
$_{15}\mathbf{S}^{\mathbf{p}}_{\mathbf{15}}$	9597.78	9592.15 ± 0.11	499	467 ± 13
$_{15}\mathbf{S}^{\mathbf{p}}_{\mathbf{16}}$	9926.89	9921.12 ± 0.16	538	515 ± 5
$_{16}S^{*}_{5}$	6836.40	6830.81 ± 0.07	581	549 ± 11
$_{16}S^{*}_{6}$	7153.68	7149.10 ± 0.09	740	590 ± 6
$_{16}S^{*}_{7}$	7474.13	7470.18 ± 0.12	800	634 ± 8
$_{16}\mathbf{S}^{\mathbf{p}}_{\mathbf{10}}$	8437.72	8433.36 ± 0.08	774	697 ± 12
$_{16}\mathbf{S}^{\mathbf{p}}_{\mathbf{11}}$	8736.46	8730.13 ± 0.27	550	444 ± 11
$_{16}\mathbf{S}^{\mathbf{p}}_{\mathbf{14}}$	9304.33	9299.32 ± 0.95	371	314 ± 6
$_{17}S^{*}_{1}$	6129.05	6128.91 ± 0.24	716	420 ± 19
$_{17}\mathbf{S}^{*}_{\mathbf{8}}$	7805.06	7802.59 ± 0.39	544	427 ± 13
$_{17}S_{12}$	9151.29	9148.44 ± 0.06	462	434 ± 10
$_{17}S_{13}$	9435.95	9428.47 ± 0.08	554	533 ± 4
$_{17}\mathbf{S}_{14}$	9709.09	9698.54 ± 0.30	462	472 ± 5
$_{17}\mathbf{S}_{15}$	9938.06	9932.67 ± 0.52	353	335 ± 3
$_{18}S^{*}_{3}$	6891.92	6888.97 ± 0.09	852	756 ± 22
$_{18}S^{*}_{4}$	7240.99	7238.54 ± 0.05	943	989 ± 3
$_{18}\mathbf{S}^{*}_{\mathbf{6}}$	7957.06	7956.81 ± 0.26	396	394 ± 14
$_{19}\mathbf{S}_{10}$	9357.40	9351.14 ± 0.05	676	616 ± 5
$_{19}\mathbf{S}_{11}$	9653.75	9644.79 ± 0.23	676	588 ± 11
$_{20}\mathbf{S}^{*}_{\mathbf{1}}$	6954.04	6953.99 ± 0.29	876	775 ± 10
$_{20}\mathbf{S}^{*}_{\mathbf{5}}$	8471.58	8465.52 ± 0.15	636	580 ± 23
$_{21}S^{*}_{6}$	8850.77	8849.07 ± 0.13	740	582 ± 7
$_{21}S^{*}_{7}$	9173.79	9171.18 ± 0.21	800	664 ± 7

Table 3. (*Continued.*)

Mode	PREM f_0	Measured f_c	PREM Q_0	Measured Q
$_{22}S^{*}_{1}$	7819.55	7822.62 ± 0.03	767	944 ± 12
$_{23}S^{*}_{4}$	8941.57	8936.44 ± 0.11	809	710 ± 8
$_{23}S^{*}_{5}$	9289.58	9289.93 ± 0.04	899	883 ± 6
$_{25}\mathbf{S}^{*}_{\mathbf{1}}$	8655.17	8656.67 ± 0.39	844	787 ± 18
$_{25}\mathbf{S}^{*}_{\mathbf{2}}$	9022.91	9025.15 ± 0.04	788	752 ± 8
$_{27}S^{*}_{2}$	9865.34	9871.92 ± 0.19	790	784 ± 4

coefficients up to higher angular order. We have also been able to improve the measurements of several modes, which are more difficult to observe and benefitted from our new data set. We will focus our discussions here on the modes which are significantly different as they are the ones that are providing us with new and improved constraints.

Fig. 5 compares splitting function measurements for five modes with the measurement of Resovsky & Ritzwoller (1998) and the prediction for S20RTS and CRUST 5.1. For these modes, our splitting functions are different than those measured by Resovsky & Ritzwoller (1998) which, we believe, is because we use a data set which is 10–20 times larger. For example, for modes $_1S_{14}$, $_2S_{12}$ and $_3S_9$ we have been able to measure splitting functions up to larger maximum angular order $s_{\max}$. Our observations are also more similar to the predictions for S20RTS + CRUST5.1 than the Resovsky & Ritzwoller (1998) measurements for these three modes. We measured all of these modes starting from PREM, so any similarity with S20RTS predictions is not because of damping towards S20RTS. We also find significant misfit reduction for our measurements as compared to the S20RTS misfit (Table 2).

Mode $_1S_{14}$ is almost a Stoneley mode (i.e. confined to the boundary between the mantle and core), and strongly sensitive to the core–mantle boundary (CMB) region (Fig. 5a). Thus, its splitting function will have an important effect on determining potential anticorrelation between $\delta v_s/v_s$ and $\delta\rho/\rho$ in the lowermost mantle. In our measurement, mode $_1S_{14}$ now shows the expected signature of a mantle-sensitive mode, with positive frequency anomalies in a ring around the Pacific surrounding negative frequency anomalies in the mid-Pacific and under Africa. This signature is also predicted by S20RTS+CRUST5.1. In contrast, the Resovsky & Ritzwoller (1998) splitting function resembles the zonal structure expected for inner-core sensitive modes, although $_1S_{14}$ is not sensitive to the inner core. We believe our observation is more representative of real mantle structure since it matches traveltimes of Sdiff. We found that we were only able to robustly measure this mode by including cross-coupling with $_0S_{21}$.

Our observed splitting function for mode $_2S_{12}$ (Fig. 5b) is very similar to the predictions by S20RTS + CRUST5.1. This mode is mainly sensitive to upper-mantle shear wave velocity v_s, which is very well predicted by S20RTS because of the use of surface waves in its construction. Thus, normal modes and surface waves give very similar structure for upper-mantle v_s. Even though there is such good agreement with S20RTS, we still find that our splitting function gives a significant additional improvement in misfit (Table 2); the S20RTS misfit is 0.37, which reduces to 0.19 for our measured splitting function. Modes $_3S_9$ and $_4S_4$ (Figs 5c and d) are also dominated by upper- and lower-mantle v_s structure and again agree well with predictions by S20RTS.

Mode $_5S_4$ (Fig. 5e) has stronger sensitivity to mantle v_p than to v_s. For this mode, the agreement with S20RTS is much lower, which is to be expected as S20RTS is a shear wave model and it indicates that

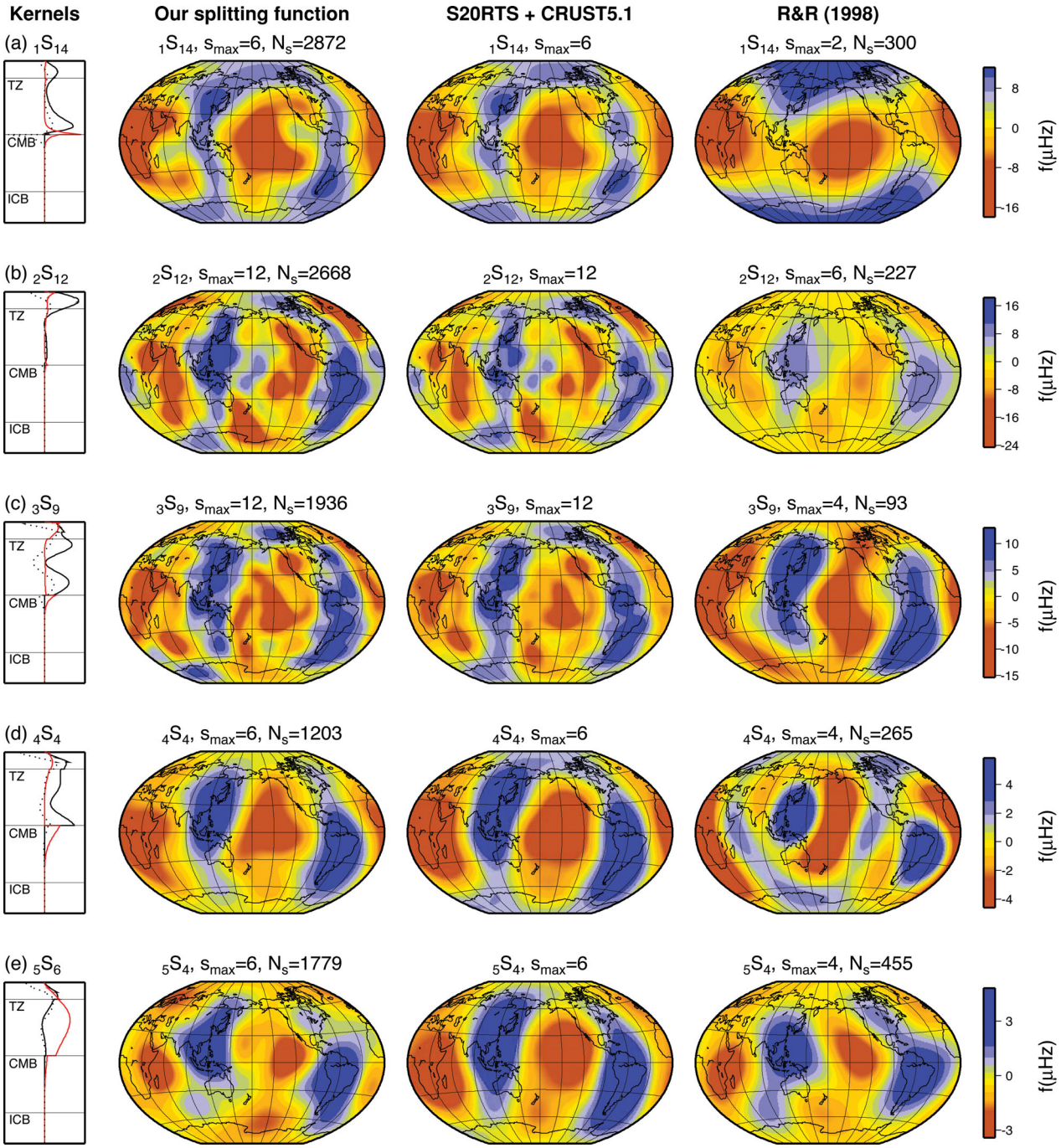

Figure 5. Our splitting function observations compared with the S20RTS + CRUST5.1 predictions and corresponding the splitting functions previously measured by Resovsky & Ritzwoller (1998) (denoted 'R&R'). For the splitting function observations, $s_{\max}$ indicates the maximum angular order of the splitting function and N_s is the number of spectra used for the inversion. All our splitting functions in this figure are measured from PREM and without knowledge of the S20RTS + CRUST5.1 predictions. Also shown are the degree $s = 0$ sensitivity kernels K_s, where the solid black line is v_s, the solid red line is v_p and the dotted line is ρ.

a constant depth scaling to get $\delta v_p/v_p$ is not correct. The PREM misfit for this mode is 0.50, which only reduces to 0.45 for the S20RTS model. A further reduction in misfit to 0.21 is obtained for our splitting function.

4.1.2 New mantle v_p sensitive modes

To improve constraints on mantle compressional velocity v_p, we investigated previously unmeasured modes with strong sensitivity to v_p. We observed strong isolated peaks for many new groups of modes in the spectra between 4 and 10 mHz. Fig. 2(a) shows angular order l versus frequency ω_k for all our measured modes, and Fig. 2(b) shows a subset of all the modes which are strongly sensitive to mantle v_p. It is obvious that these modes form 'branches' that cross-cut the conventional overtone branches with constant n, but can still be ordered in terms of increasing angular order l. Fig. 6 shows sensitivity kernels for four branches, which differ by the number of maxima in the v_p mantle sensitivity kernels.

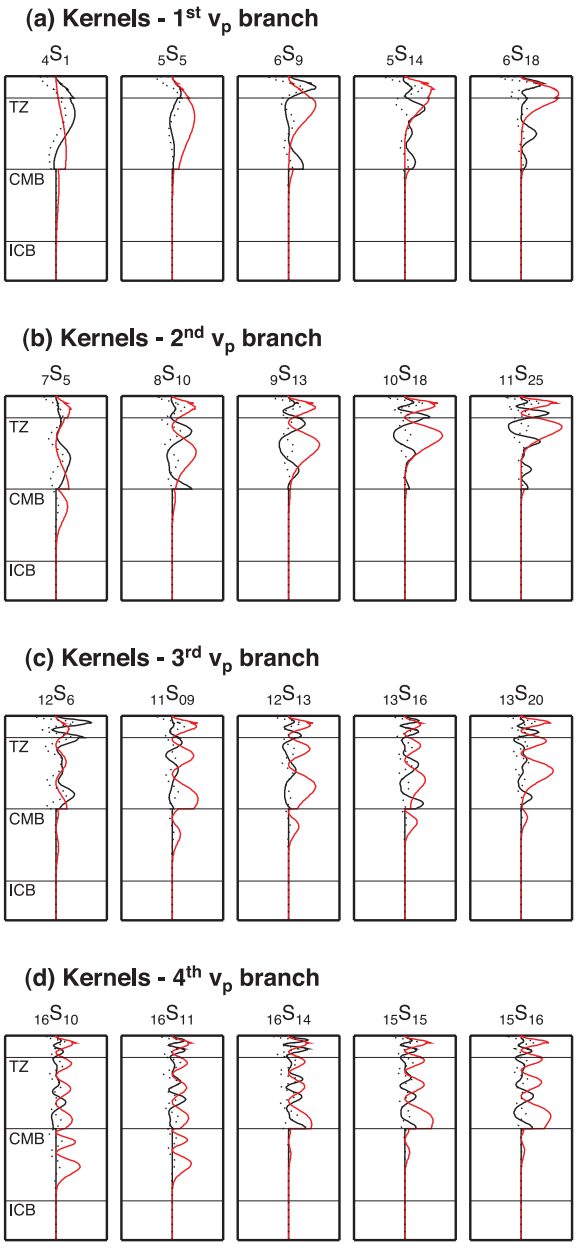

Figure 6. Sensitivity kernels for angular order $s = 0$ for representative modes of the first four v_p mantle branches, where the solid red line is the v_p sensitivity, the solid black line is v_s and the dotted line is ρ. (a) First branch with one maximum in the mantle for the v_p sensitivity, (b) second branch with two maxima, (c) third branch with three maxima and (d) fourth branch with four maxima. Additional maxima exist in the outer core for some of the modes.

The first v_p branch has one maximum in the mantle, the second v_p branch has two maxima etc. The branches behave in the same way as conventional mode branches, i.e. the sensitivity kernels of a given branch vary smoothly with angular order l and the sensitivity kernels of each branch increase near Earth's surface for the larger values of l, similar to the standard fundamental branch ${}_0S_l$. Table 3 shows the centre frequency and Q measurements for the v_p sensitive modes. We observe that for the first branch, our Q measurements are all larger than the PREM predictions, while for the fourth branch our Q measurements are smaller than PREM. These provide new constraints on the radial variations of Q_μ and Q_κ in the mantle.

We measured 33 new mantle v_p sensitive modes which had not been measured before. It is therefore important to test whether our measurements are robust, especially at these relatively high frequencies, and whether potential interference with other modes has been taken into account properly. It is useful to check branch consistency of the splitting function coefficients. The sensitivity kernels only change smoothly with increasing l (Fig. 6), so we expect that the coefficients vary smoothly with increasing l. We found that this is indeed the case for all our v_p branches modes. Fig. 7 shows the branch consistency for the $s = 2$ coefficients of the first three v_p sensitive branches. Also shown are the predictions for shear wave velocity models S20RTS and S40RTS (Ritsema *et al.*, 1999, 2011) which are scaled to get compressional mantle velocity. We find that neither of these two models predict the v_p sensitive modes well, which is not surprising as these modes were not included in the construction of these models. Also, these models assume a constant scaling between $\delta v_s/v_s$ and $\delta v_p/v_p$, and our new observations of v_p sensitive modes shows that this is not the case providing new constraints on the compressional structure of the lower mantle.

Fig. 8 shows one example splitting function map for each of the v_p branches. Overall, the splitting functions show the expected 'ring around the Pacific' as is also predicted by S20RTS + CRUST5.1. The consistency of these features across all four observed splitting functions, indicates that our measurements are robust. This is especially encouraging as these modes are measured in different groups and frequency ranges and some in the self-coupling approximation and others are cross-coupled to close lying neighbouring modes. However, there are also consistent differences between our measurements and the S20RTS mantle predictions. This is evident in the misfit calculations (see Table 1), which are all much larger for the S20RTS predictions than for our splitting function measurement. For example, for mode ${}_5S_{14}$ the S20RTS misfit is 1.23, which reduces to 0.29 for our measured splitting function. Differences can also be seen in the splitting function maps of Fig. 8. A high-frequency anomaly extends across Asia and Northern Europe in ${}_5S_{14}$, ${}_{12}S_{13}$ and ${}_{15}S_{16}$, which is not as strong in the predictions. Another high-frequency anomaly in the South Pacific just South of 30°S also is not seen so strongly in the predictions. The predictions are obtained by using a constant depth scaling between $\delta v_s/v_s$ and $\delta v_p/v_p$, which clearly cannot fully explain our newly measured v_p sensitive modes.

4.1.3 Odd-degree mantle structure

The generalized splitting function technique also allows for the analysis of cross-coupled modes, and hence provide information on odd-degree structure. We included cross-coupling for most groups of modes in Table 2, but will discuss only the ones for which the measured splitting functions are robust. Some cross-coupled structure coefficients were measured by Resovsky & Ritzwoller (1998) and we find that our results for modes pairs such as ${}_1S_5-{}_2S_4$ and ${}_1S_6-{}_2S_5$ are very similar to their results. We have made measurements of the same 10 cross-coupled modes as Resovsky & Ritzwoller (1998) and added a total of 18 new cross-coupled mantle-sensitive splitting functions of which 12 provide information on odd-degree structure. There are now a total of 18 mantle-sensitive odd-degree splitting functions available. In addition to odd-degree structure, we have also measured a total of 10 cross-coupled

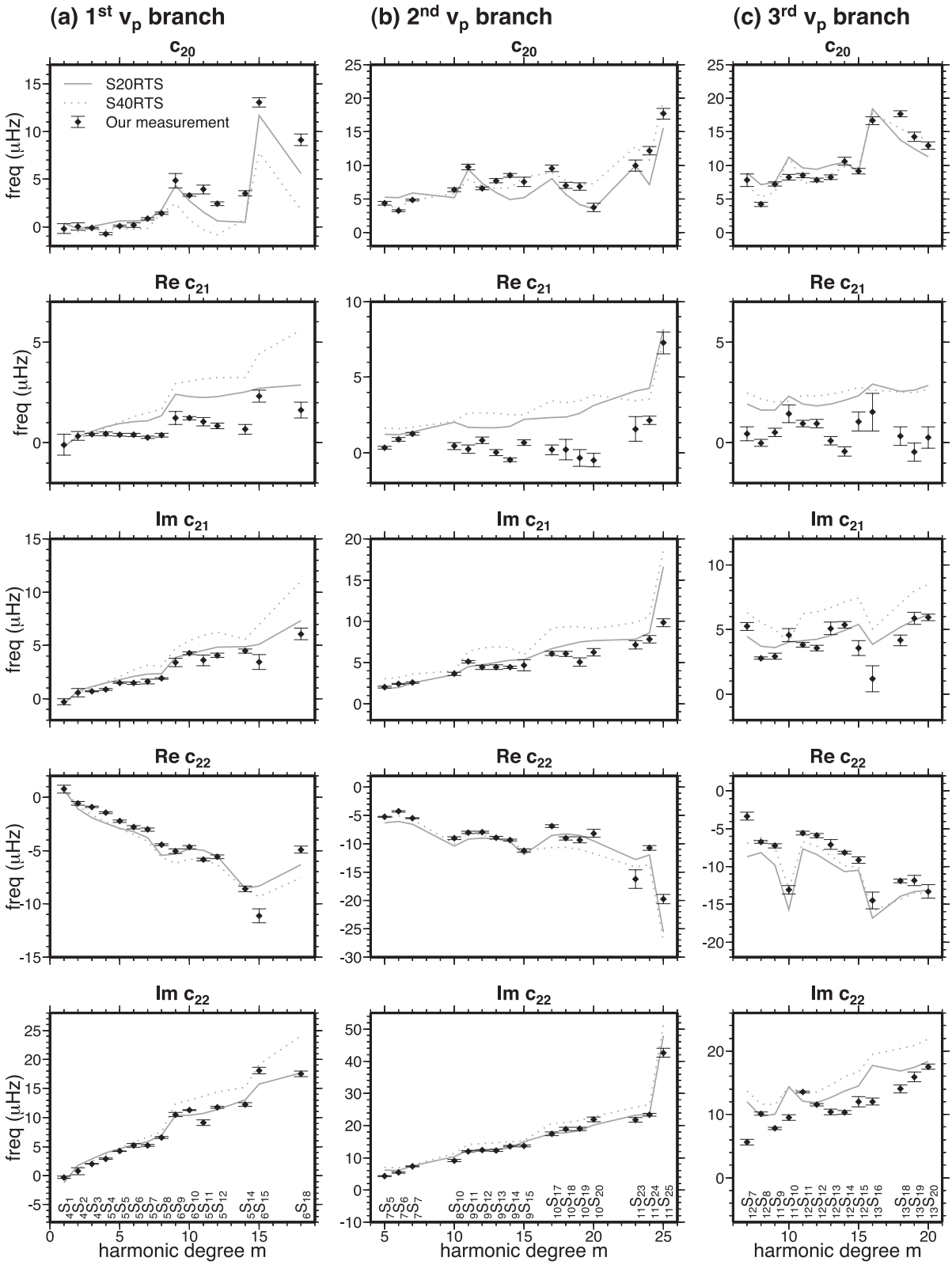

Figure 7. Our measured values for degree $s = 2$ splitting function coefficients for three branches of mantle v_p sensitive modes (black diamonds). Also shown are the predictions for models S20RTS (grey solid line) and S40RTS (grey dotted line).

splitting functions which are sensitive to even-degree mantle structure.

Fig. 9 shows examples of our new cross-coupled odd-degree splitting functions. The overall pattern of our observed splitting functions is similar to the S20RTS + CRUST5.1 predictions. However, there are also significant differences which are larger than seen in the even-degree self-coupled splitting functions (Fig. 5 and 8). Constraints on odd-degree mantle structure in S20RTS come

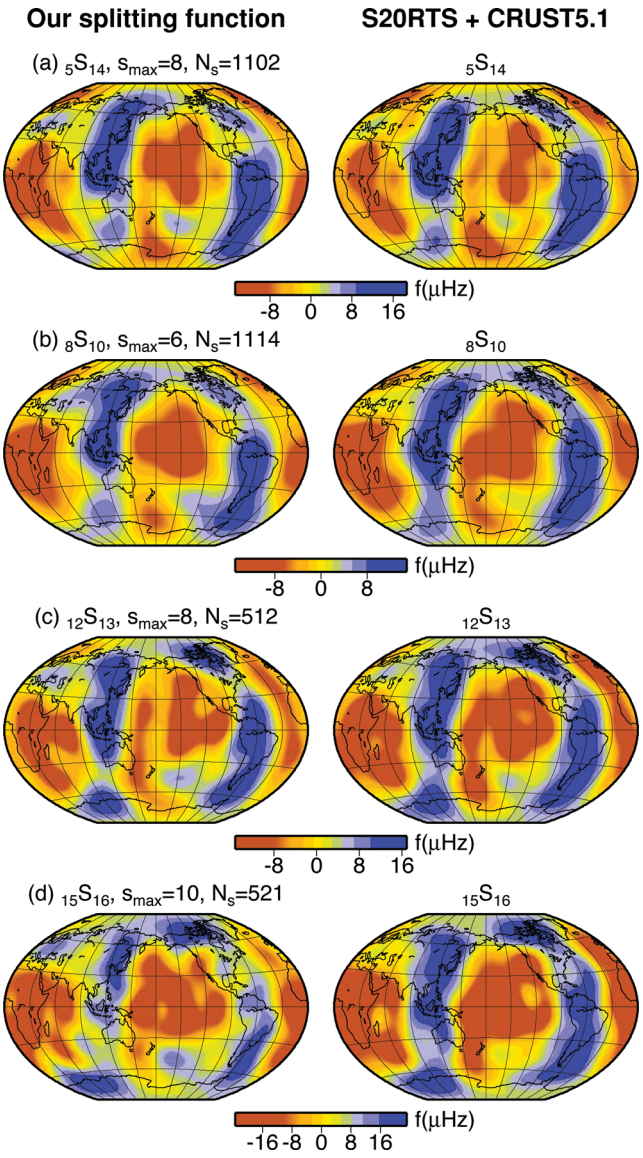

Figure 8. Our splitting function observations for mantle v_p sensitive modes which have not been measured before. Also shown are the S20RTS + CRUST5.1 predictions. Sensitivity kernels for these modes are shown in Fig. 6.

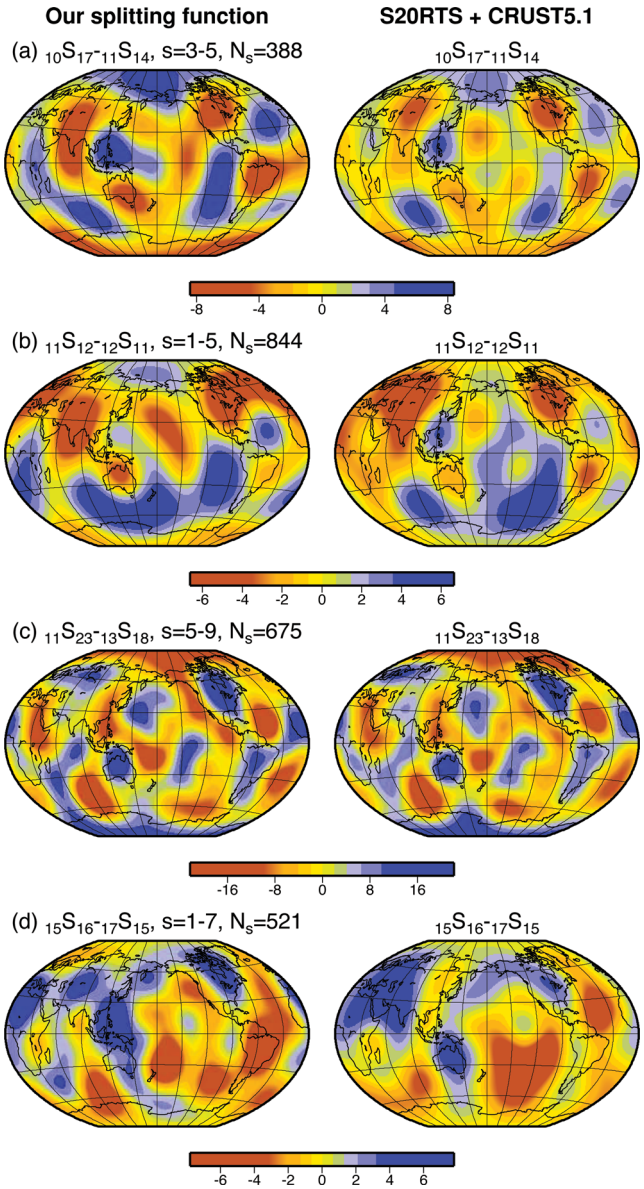

Figure 9. Our splitting function observations for odd-degree cross-coupled mantle sensitive modes which have not been measured before. Also shown are the S20RTS + CRUST5.1 predictions. The angular order range of the splitting function of each mode pair is denoted by s.

from surface waves and body waves only, so it is not surprising that the longest period odd-degree normal-mode structure is not as well predicted by S20RTS.

4.2 Inner-core sensitive modes

Observations of the splitting of inner-core sensitive modes have been used extensively to study the anisotropic structure of the Earth's inner core (Woodhouse *et al.* 1986; Tromp 1993; Beghein & Trampert 2003). We have found that we were not able to make robust measurements for some previously measured inner-core sensitive modes. Mode $_6S_1$ was only measured by Resovsky & Ritzwoller (1998), but we found that there was no signal visible in individual data spectra, not even for large and deep earthquakes such as the Bolivia 1994 event. For modes $_{21}S_8$ and $_{27}S_1$, we found that the c_{20} coefficients in particular are poorly constrained. On the other hand, we were able to measure several new inner-core sensitive modes which had not been measured before. These are $_{11}S_1$, $_{11}S_6$, $_{13}S_6$, $_{15}S_4$, $_{17}S_8$, $_{18}S_6$, $_{20}S_1$, $_{20}S_5$, $_{25}S_1$ and $_{25}S_2$. We have also made a new measurement for mode $_{16}S_6$, which was measured before by Widmer *et al.* (1992), but not by the more recent studies of He & Tromp (1996) and Durek & Romanowicz (1999). We find that all of our newly measured modes (except for $_{15}S_4$) have a lower measured Q than predicted by PREM, suggesting that the inner core may be more strongly attenuating than previously thought.

Fig. 2(c) shows the angular order versus frequency of all our measured inner-core sensitive modes. Just like mantle-sensitive modes, the inner-core sensitive modes are divided into modes mainly sensitive to v_s, also called 'PKJKP' modes, and modes mainly sensitive to v_p but also with some v_s sensitivity, the 'PKIKP' modes (Deuss, 2008). For a given overtone number n, the low angular order l modes

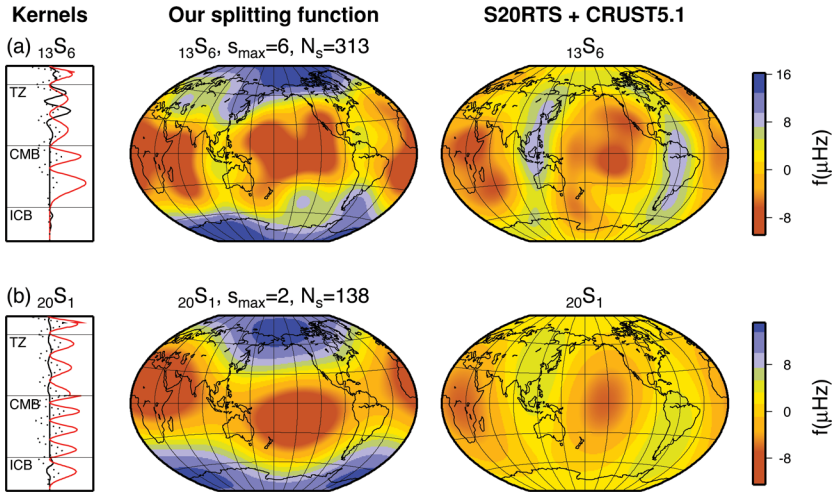

Figure 10. Our splitting function observations for two inner-core sensitive modes which have not been measured before. Also shown are the S20RTS + CRUST5.1 predictions and the sensitivity kernels, where the solid black line is v_s, the solid red line is v_p and the dotted line is ρ.

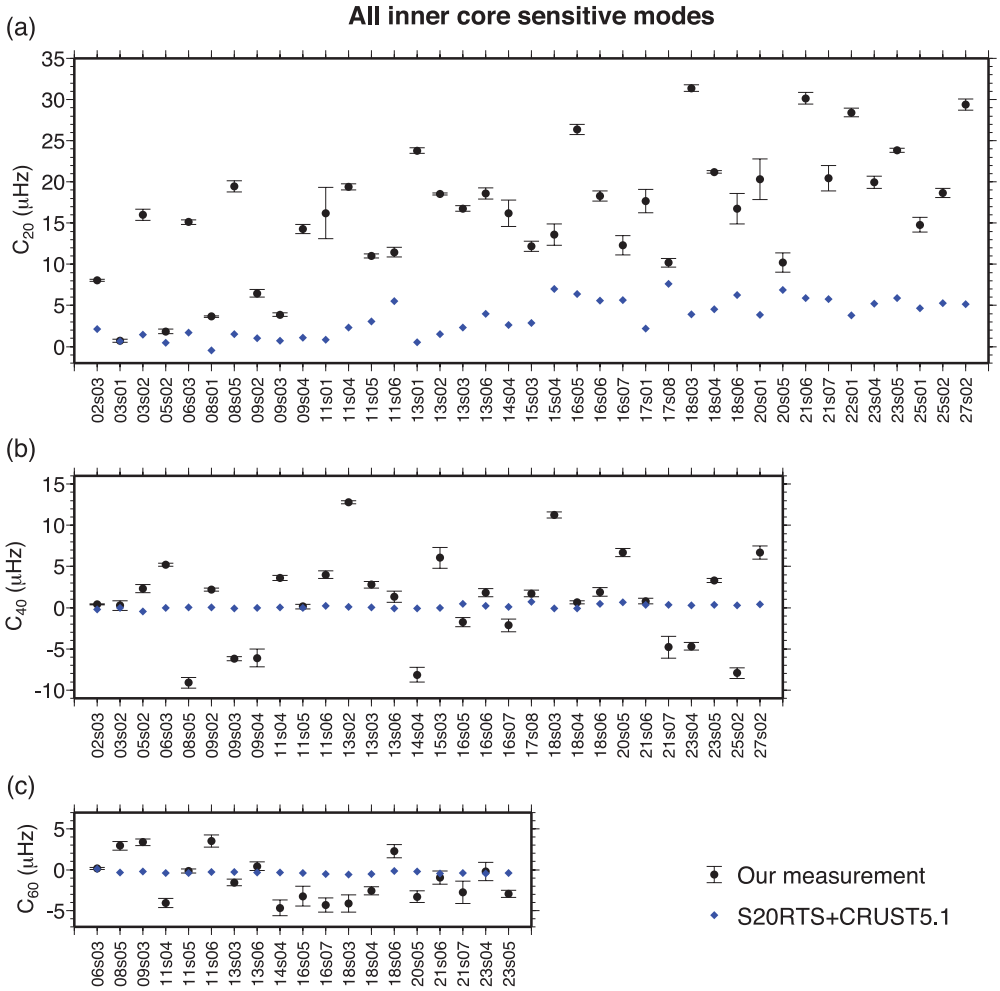

Figure 11. Coefficients (a) c_{20}, (b) c_{40} and (c) c_{60} for inner-core sensitive modes measured in this study. Also shown are the S20RTS + CRUST5.1 predictions.

are 'PKIKP' (or v_p) modes and the signature changes to 'PKJKP' (or v_s) modes for increasing angular order.

Fig. 10 shows splitting function observations for two inner-core sensitive modes which have not been measured before. Mode $_{13}S_6$ (Fig. 10a) is a 'PKJKP' mode with small v_s sensitivity to the inner core. This mode shows the typical 'zonal' structure which is seen in inner-core sensitive modes; this zonal structure is not seen in the S20RTS + CRUST5.1 predictions. Mode $_{20}S_1$ is a 'PKIKP' mode (Fig. 10b) with strong sensitivity to v_p, and again displays zonal structure which cannot be matched by S20RTS + CRUST5.1.

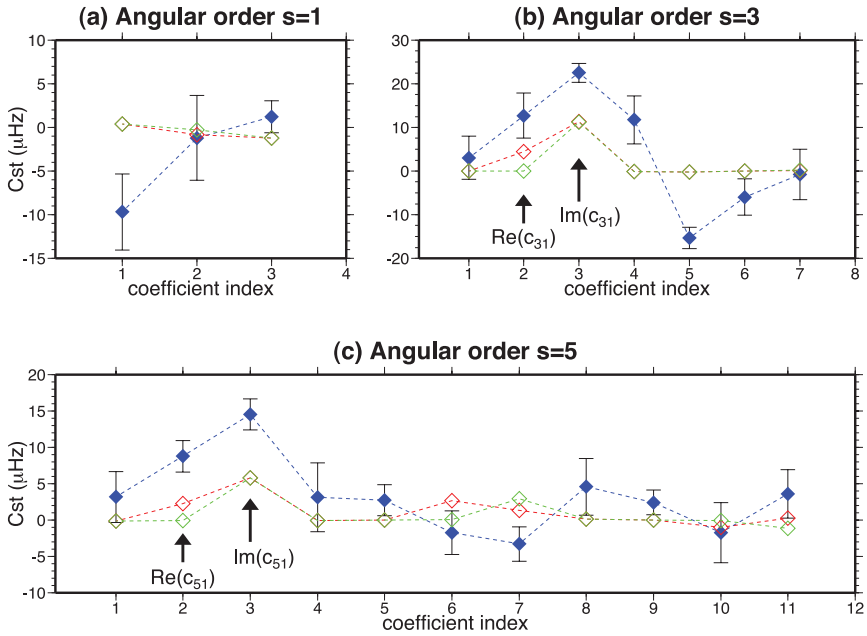

Figure 12. Our splitting function observations for odd-degree inner-core sensitive cross-coupled pair ${}_{16}S_5 - {}_{17}S_4^J$. For $s = 1$, the index (1,2,3) relates to c_{10}, Re(c_{11}), Im (c_{11}). For $s = 3$ the index (1,2,3,4,5, . . .) relates to c_{30} , Re(c_{31}), Im (c_{31}), Re(c_{32}), Im (c_{32}), . . . etc. The blue diamonds indicate our measurements (as plotted in Fig. 13a), the green diamonds denote model predictions for hemispherical boundaries at 0° and 180° and the red diamonds for hemisphere boundaries at 14°E and 151°W. The predictions are for the inner-core anisotropy model of Durek & Romanowicz (1999).

All our inner-core sensitive modes show zonal structure which is due to anomalous c_{20} coefficients, which cannot be explained by mantle structure only and thus require the presence of inner-core anisotropy (see Fig. 11a). It has been well known from previous splitting function studies that the c_{20} and c_{40} coefficients of inner-core sensitive modes are strongly underpredicted by mantle models only (Woodhouse *et al.* 1986; He & Tromp 1996; Durek & Romanowicz 1999), while the other coefficients are close to mantle predictions. These anomalous coefficients have been attributed to inner-core anisotropy. In particular, cylindrical anisotropy with its symmetry axis aligned with the Earth's rotation axis explains the 'zonal splitting' seen in these coefficients (Woodhouse *et al.* 1986; Tromp 1995), in agreement with body-wave traveltimes observations of inner-core anisotropy (i.e. Morelli *et al.* 1986; Creager 1999). Here, we show for the first time that the c_{60} coefficients are also anomalous (Fig. 11c). Whereas the c_{20} coefficients are always positive in sign, the c_{40} and c_{60} coefficients have positive and negative values. The new modes and the c_{60} coefficients will provide improved constraints in future models of inner-core anisotropy.

4.2.1 Odd-degree inner-core structure

Cross-coupling between inner-core sensitive modes allows for measuring hemispherical structure in inner-core anisotropy (Deuss *et al.*, 2010), which had been observed in body-wave studies only (Tanaka & Hamaguchi, 1997; Niu & Wen, 2001; Irving & Deuss, 2011). Hemispherical structure is odd-degree, and therefore can only be observed using cross-coupled modes (Irving *et al.* 2009). Such coupling was shown to be strong for pairs of modes where one is an observable inner-core sensitive mode, and the other one is an inner-core confined oscillation (denoted *J* in Table 1). We calculate splitting function coefficients for hemispherical inner-core anisotropy using the theory of Irving *et al.* (2009). If cylindrical anisotropy is present in the Western Hemisphere only with boundaries at 0° and 180° longitude, then the odd-degree coefficients are dominated by Im (c_{31}) and Im (c_{51}) (see Fig. 12). These are the odd-degree equivalents of the dominant c_{20} and c_{40} coefficients in the self-coupling measurements of inner-core sensitive modes. For the hemispheres boundaries at longitudes of 14°E and 151°W, additional coefficients Re(c_{31}) and Re(c_{51}) appear.

Deuss *et al.* (2010) reported observations for the three pairs of modes ${}_8S_5 - {}_5S_{10}^J$, ${}_{14}S_4 - {}_{11}S_7$ and ${}_{16}S_5 - {}_{17}S_4^J$ (which have been repeated here for completeness, see Fig. 13a–c). In this study, we have added one more pair of cross-coupled inner-core sensitive modes, that is, ${}_{11}S_1 - {}_8S_4^J$ (Fig. 13d). For these pairs, we first measure the splitting function without cross-coupling and calculate the corresponding misfit. We then add cross-coupling for odd-degree structure and for each pair the misfit significantly improves. Thus, we believe that all these mode pairs robustly show hemispherical structure in their cross-coupled splitting function. Fig. 13 shows the observed odd-degree splitting functions for these four mode pairs, compared with predictions for mantle structure only. Similarly to what is seen in Fig. 10, mantle structure cannot explain the strong antisymmetric zonal splitting which is observed in the real data splitting function.

5 DISCUSSION AND CONCLUSIONS

We have measured a new data set of 196 normal-mode splitting functions, of which 92 had not been measured before. Our splitting function coefficients can be found online at http://bullard.esc.cam.ac.uk/~deuss/research/splitting-functions/ and are also available as online supplement at *Geophysical Journal International*. Previous data sets were dominated by modes sensitive to mantle shear wave velocity or inner-core structure. Our data set contains 33 new modes which are mainly sensitive to compressional

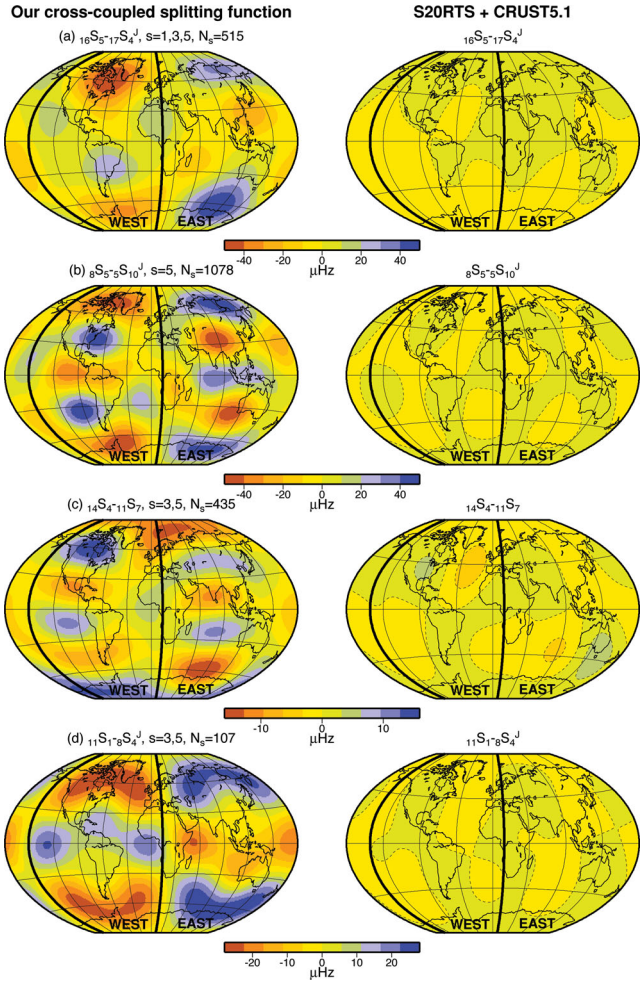

Figure 13. Our splitting function observations for odd-degree cross-coupled inner-core sensitive modes. Also shown are the S20RTS + CRUST5.1 predictions. The angular order range of the splitting function of each mode pair is denoted by s. The black solid lines denote the hemisphere boundaries at 14° E and 151° W, as seen in body wave observations (Irving & Deuss, 2011).

wave velocity in the mantle, which will provide new constraints on the upper- and lower-mantle compressional structure and on the scaling ratio between $\delta v_s/v_s$ and $\delta v_p/v_p$. We have also significantly expanded the number of cross-coupled odd-degree splitting functions with mantle sensitivity to a total of 18. This quantity of odd-degree splitting functions will make it feasible to constrain odd-degree mantle structure using splitting functions. Finally, we added 10 new inner-core sensitive splitting functions and found that anomalous zonal structure, representative of inner-core anisotropy, is also present at degree 6 (i.e. c_{60}), in addition to degrees 2 and 4 (i.e. c_{20} and c_{40}).

ACKNOWLEDGEMENTS

AD has been funded by the European Research Council under the European Community's Seventh Framework programme (FP7/2007-2013)/ERC grant agreement 204995 and by a Philip Leverhulme Prize. JR is supported by NSF grant EAR-0944167. We thank Mike Ritzwoller, Gabi Laske and an anonymous reviewer for constructive comments which helped to improve the manuscript. The facilities of the IRIS Data Management System, and specifically the IRIS Data Management Center, were used for access to waveform and metadata required in this study. We also acknowledge use of the 'Global CMT project' webpage for the earthquake source parameters used in this study.

REFERENCES

Beghein, C. & Trampert, J., 2003. Robust normal mode constraints on inner-core anisotropy from model space search, *Science,* **299,** 552–555.

Creager, K., 1999. Large-scale variations in inner core anisotropy, *J. geophys. Res.,* **104**(B10), 23 127–23 139.

Dahlen, F.A., 1968. The normal modes of a rotating, elliptical Earth, *Geophys. J. R. astr. Soc.,* **16,** 329–367.

Dahlen, F.A., 1969. The normal modes of a rotating, elliptical Earth, II, near resonant multiplet coupling, *Geophys. J. R. astr. Soc.,* **18,** 397–436.

Dahlen, F.A., 1982. The effect of data windows on the estimation of free oscillation parameters, *Geophys. J. R. astr. Soc.,* **69**(2), 537–549.

Dahlen, F.A. & Tromp, J., 1998. *Theoretical Global Seismology*. Princeton University Press, Princeton, NJ.

Deuss, A., 2008. Normal mode constraints on shear and compressional wave velocity of the Earth's inner core, *Earth planet. Sci. Lett.,* **268**(3–4), 364–375.

Deuss, A. & Woodhouse, J., 2001. Theoretical free-oscillation spectra: the importance of wide band coupling, *Geophys. J. Int.,* **146**(3), 833–842.

Deuss, A., Irving, J.C.E. & Woodhouse, J.H., 2010. Regional variation of inner core anisotropy from seismic normal mode observations, *Science,* **328**(5981), 1018–1020.

Deuss, A., Ritsema, J. & Heijst, H.V., 2011. Splitting function measurements for Earth's longest period normal modes using recent large earthquakes, *Geophys. Res. Lett.,* **38**(4), L04303, doi:10.1029/2010GL046115.

Durek, J.J. & Romanowicz, B., 1999. Inner core anisotropy inferred by direct inversion of normal mode spectra, *Geophys. J. Int.,* **139,** 599–622.

Dziewonski, A.M. & Anderson, D.L., 1981. Preliminary reference Earth model, *Phys. Earth planet. Inter.,* **25**(4), 297–356.

Edmonds, A.R., 1960. *Angular Momentum and Quantum Mechanics*. Princeton University Press, Princeton, NJ.

Giardini, D., Li, X.-D. & Woodhouse, J.H., 1987. Three dimensional structure of the earth from splitting in free oscillation spectra, *Nature,* **325,** 405–411.

Giardini, D., Li, X.-D. & Woodhouse, J.H., 1988. Splitting functions of long-period normal modes of the Earth, *J. geophys. Res.,* **93,** 13 716–13 742.

He, X. & Tromp, J., 1996. Normal-mode constraints on the structure of the Earth, *J. geophys. Res.,* **101,** 20 053–20 082.

Irving, J.C.E. & Deuss, A., 2011. Hemispherical structure in inner core velocity anisotropy, *J. geophys. Res.,* **116**(B4), B04307, doi:10.1029/2010JB007942.

Irving, J.C.E., Deuss, A. & Woodhouse, J.H., 2009. Normal mode coupling due to hemispherical anisotropic structure in Earth's inner core, *Geophys. J. Int.,* **178**(2), 962–975.

Ishii, M. & Tromp, J., 1999. Normal-mode and free-air gravity constraints on lateral variations in velocity and density of the Earth's mantle, *Science,* **285,** 1231–1236.

Kuo, C. & Romanowicz, B., 2002. On the resolution of density anomalies in the earth's mantle using spectral fitting of normal-mode data, *Geophys. J. Int.,* **150,** 162–179.

Li, X.-D., Giardini, D. & Woodhouse, J.H., 1991. Large scale three dimensional even degree structure of the Earth from splitting of long period normal modes, *J. geophys. Res.,* **96,** 551–577.

Masters, G., Bolton, G.L.H. & Dziewonski, A., 2000a. The relative behaviour of shear velocity, bulk sound speeds, and compressional velocity in the mantle: implication for chemical and thermal structure, eds Karato, S. *et al.*, Geophysical Monograph, AGU, Washington, **117,** 63–87.

Masters, G., Laske, G. & Gilbert, F., 2000b. Matrix autoregressive analysis of free-oscillation coupling and splitting, *Geophys. J. Int.,* **143,** 478–489.

Mooney, W.D., Laske, G. & Masters, G., 1998. A new global crustal model at 5 x 5 degrees: CRUST5.1, *J. geophys. Res.,* **103,** 727–747.

Morelli, A., Dziewonski, A.M. & Woodhouse, J.H., 1986. Anisotropy of the inner core inferred from PKIKP travel times, *Geophys. Res. Lett.,* **13,** 1545–1548.

Niu, F. & Wen, L., 2001. Hemispherical variations in seismic velocity at the top of the Earth's inner core, *Nature,* **410**(6832), 1081–1084.

Nolet, G. & Kennett, B., 1987. Normal-mode representations of multiple-ray reflections in a spherical Earth, *Geophys. J. R. astr. Soc.,* **53**(2), 219–226.

Resovsky, J.S. & Pestana, R., 2003. Improved normal mode constraints on lower mantle vp from generalized spectral fitting, *Geophys. Res. Lett.,* **30**(7), 1383, doi:10.1029/2002GL015790.

Resovsky, J. & Ritzwoller, M., 1998. New and refined constraints on three-dimensional Earth structure from normal modes below 3 mHz, *J. Geophys. Res.-Sol. Earth,* **103**(B1), 783–810.

Resovsky, J.S. & Ritzwoller, M.H., 1999a. A degree 8 shear velocity model from normal mode observations below 3 mHz, *J. geophys. Res.,* **104,** 993–1014.

Resovsky, J.S. & Ritzwoller, M.H., 1999b. Regularization uncertainty in density models estimated from normal mode data, *Geophys. Res. Lett.,* **26,** 2319–2322.

Resovsky, J. & Trampert, J., 2003. Using probabilistic seismic tomography to test mantle velocity-density relationships, *Earth planet. Sci. Lett.,* **215**(1–2), 121–134.

Ritsema, J., van Heijst, H. & Woodhouse, J., 1999. Complex shear wave velocity structure imaged beneath Africa and Iceland, *Science,* **286,** 1925–1928.

Ritsema, J., Deuss, A., van Heijst, H.J. & Woodhouse, J.H., 2011. S40RTS: a degree-40 shear-velocity model for the mantle from new rayleigh wave dispersion, teleseismic traveltime and normal-mode splitting function measurements, *Geophys. J. Int.,* **184**(3), 1223–1236.

Ritzwoller, M., Masters, G. & Gilbert, F., 1986. Observations of anomalous splitting and their interpretation in terms of aspherical structure, *J. geophys. Res.,* **91,** 10 203–10 228.

Ritzwoller, M., Masters, G. & Gilbert, F., 1988. Constraining aspherical structure with low-degree interaction coefficients: application to uncoupled multiplets, *J. geophys. Res.,* **93,** 6369–6396.

Romanowicz, B., 2001. Can we resolve 3D density heterogeneity in the lower mantle? *Geophys. Res. Lett.,* **28**(6), 1107–1110.

Tanaka, S. & Hamaguchi, H., 1997. Degree one heterogeneity and hemispherical variation of anisotropy in the inner core from PKP(BC)-PKP(DF) times, *J. geophys. Res.,* **102**(B2), 2925–2938.

Tarantola, A. & Valette, B., 1982. Generalized nonlinear inverse problems solved using the least squares criterion, *Rev. Geophys.,* **20(2),** 213–232.

Trampert, J., Deschamps, F., Resovsky, J. & Yuen, D., 2004. Probabilistic tomography maps chemical heterogeneities throughout the lower mantle, *Science,* **306**(5697), 853–856.

Tromp, J., 1993. Support for anisotropy of the Earth's inner core from free oscillations, *Nature,* **366,** 678–681.

Tromp, J., 1995. Normal-mode splitting due to inner-core anisotropy, *Geophys. J. Int.,* **121,** 963–968.

Widmer, R., Masters, G. & Gilbert, F., 1992. Observably split multiplets-data analysis and interpretation in terms of large-scale aspherical structure, *Geophys. J. Int.,* **111,** 559–576.

Woodhouse, J.H., 1980. The coupling and attenuation of nearly resonant multiplets in the Earth's free oscillation spectrum, *Geophys. J. R. astr. Soc.,* **61,** 261–283.

Woodhouse, J.H. & Dahlen, F.A., 1978. The effect of a general aspherical perturbation on the free oscillations of the Earth, *Geophys. J. R. astr. Soc.,* **53,** 335–354.

Woodhouse, J.H. & Giardini, D., 1985. Inversion for the splitting function of isolated low order normal mode multiplets, *EOS, Trans. Am. geophys. Un.,* **66,** 300.

Woodhouse, J.H., Giardini, D. & Li, X.D., 1986. Evidence for inner core anisotropy from free oscillations, *Geophys. Res. Lett.,* **13,** 1549–1552.

SUPPORTING INFORMATION

Additional Supporting Information may be found in the online version of this article:

cst-coef.dat
cst-coef-cross.dat (http://gji.oxfordjournals.org/lookup/suppl/doi:10.1093/gji/ggt010/-/DC1)

Please note: Oxford University Press are not responsible for the content or functionality of any supporting materials supplied by the authors. Any queries (other than missing material) should be directed to the corresponding author for the article.